Remote Sensing of Environment 260 (2021) 112441

Contents lists available at ScienceDirect

Remote Sensing of Environment

journal homepage: www.elsevier.com/locate/rse

Joint exploitation of space-borne and ground-based multitemporal InSAR measurements for volcano monitoring: The Stromboli volcano case study

Federico Di Traglia [a], Claudio De Luca [b], Mariarosaria Manzo [b], Teresa Nolesini [c], Nicola Casagli [a,d], Riccardo Lanari [b], Francesco Casu [b,*]

[a] Università degli Studi di Firenze, Dipartimento di Scienze della Terra, Via La Pira 4, 50121 Firenze, Italy
[b] IREA-CNR, Via Diocleziano 328, 80124, Napoli – Via Bassini 15, 20133 Milano, Italy
[c] Università degli Studi di Firenze, Centro per la Protezione Civile, Piazza San Marco 4, 50121 Firenze, Italy
[d] National Institute of Oceanography and Applied Geophysics - OGS, Trieste, Italy

ARTICLE INFO

Keywords:
InSAR
GB-InSAR
Sentinel-1
Stromboli
Data-fusion
P-SBAS

ABSTRACT

We present a joint exploitation of space-borne and ground-based Synthetic Aperture Radar Interferometry (InSAR) and Multi Temporal (MT) InSAR measurements for investigating the Stromboli volcano (Italy) deformation phenomena. In particular, we focus our analysis on three periods: a) the time interval following the 2014 flank eruption, b) the July–August 2019 eruption and c) the following post-eruptive phase. To do this, we take advantage from an unprecedented set of space-borne and ground-based SAR data collected from April 2015 up to November 2019 along two (one ascending and one descending) Sentinel-1 (S-1) tracks, as well as, in the same period, by two ground-based systems installed along the Sciara del Fuoco northern rim. Such data availability permitted us to first characterize the volcano long-term 3D deformation behavior of the pre-eruptive period (April 2015–June 2019), by jointly inverting the space-borne and ground-based InSAR measurements. Then, the GB-SAR measurements allowed us to investigate the sin-eruptive time span (3rd July 2019 – 30th August 2019) which revealed rapid deformation episodes (e.g. more than 30 mm/h just 2 min before the 3rd July 2019 explosion) associated with the eruptive activity, that cannot be detected with the weekly S-1 temporal sampling. Finally, the S-1 measurements permitted to better constrain the post 2019 eruption deformations (31st August 2019 – 5th November 2019), which are mainly located outside the GB-SAR sensed area. The presented results demonstrate the effectiveness of the joint exploitation of the InSAR measurements obtained through satellite and terrestrial SAR systems, highlighting their strong complementarity to map and interpret the deformation phenomena affecting volcanic areas.

1. Introduction

Geodetic techniques are powerful methods for determining the current state of magmatic/volcanic systems, which have been significantly extended using Synthetic Aperture Radar (SAR) data (Pritchard and Simons, 2004; Sansosti et al., 2010; Chaussard and Amelung, 2012; Biggs et al., 2014; Pinel et al., 2014; Ebmeier et al., 2018; Dumont et al., 2018; Dzurisin et al., 2019; Biggs and Wright, 2020). Space-borne SAR data and, in particular, the Differential and/or Multi-Temporal Interferometry (InSAR and MT-InSAR) techniques, are very useful for determining the extent and current state of a volcano slope instability that manifests in many forms, ranging from steady state to punctuated movement, or shallow erosion to deep-seated spreading (Amelung and Day, 2002; Borgia et al., 2000, 2005; Neri et al., 2009; Bonforte et al., 2011; Ruch et al., 2013; Schaefer et al., 2015, 2019). Interpreting InSAR-derived ground deformation signals associated to volcano slope instability is still challenging, being related to i) pressure changes due to magma movement (Bonforte and Guglielmino, 2015; Froger et al., 2015; Richter and Froger, 2020) or variations in hydrothermal systems (Narita and Murakami, 2018); ii) persistent, deep-seated flank motion (Lundgren et al., 2004; Bonforte et al., 2011; Chen et al., 2017; Poland et al., 2017; Di Traglia et al., 2018a); iii) localized ground motion related to shallow erosion or accumulation (Di Traglia et al., 2018b); iv) thermal contraction or subsidence of newly emplaced lava or tephra deposits (Chaussard, 2016; McAlpin et al., 2017; Chen et al., 2018; Schaefer et al., 2019).

* Corresponding author.
E-mail address: casu.f@irea.cnr.it (F. Casu).

https://doi.org/10.1016/j.rse.2021.112441
Received 4 August 2020; Received in revised form 31 March 2021; Accepted 4 April 2021
Available online 17 April 2021

Although their potential and applicability have been already widely testified in several contexts, space-borne InSAR and MT-InSAR, as any radar system, allow measuring one-dimensional (1D) ground motion along the sensor line of sight (LOS) direction (Franceschetti and Lanari, 1999). This implies that, due to the use of nearly polar orbit satellites, the space-borne InSAR sensors are essentially unable to detect the ground displacements along the North-South direction. However, several solutions have been developed to increase the ability to solve the whole (3D) displacement field (Hu et al., 2014), either integrating InSAR/MT-InSAR measurements with those obtained from techniques capable of extrapolating information on ground displacement from the amplitude of the SAR images, such as the pixel-offset (Casu et al., 2011) and the Multi-Aperture InSAR (Bechor and Zebker, 2006), or coupling InSAR/MT-InSAR with GNSS (Global Navigation Satellite System) and/or other geodetic techniques (Fernández et al., 2003; Guglielmino et al., 2011; Muller et al., 2015; Garthwaite et al., 2019; Smittarello et al., 2019).

In the recent years, ground-based (GB) SAR, using InSAR technology

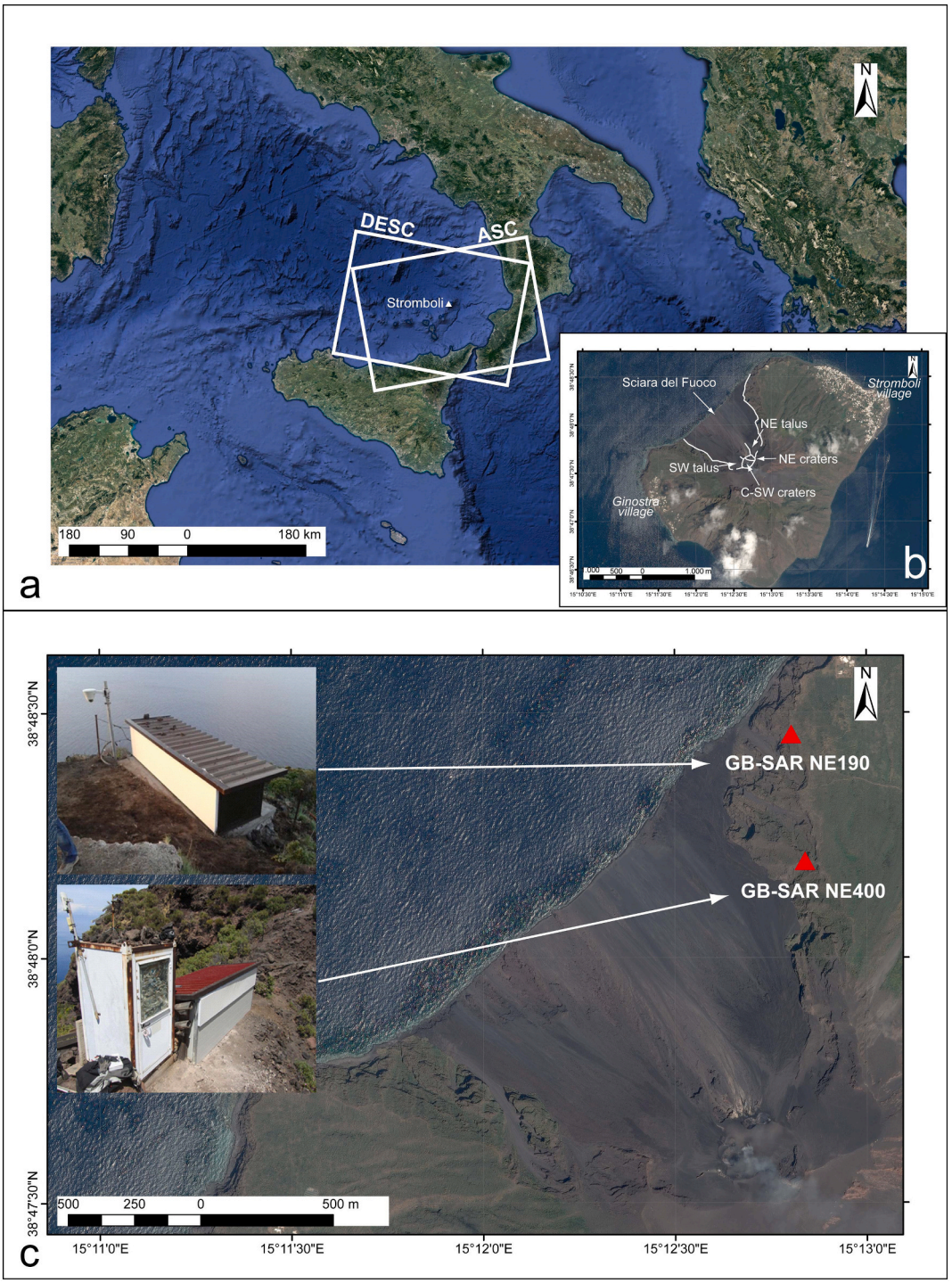

Fig. 1. The Stromboli Island actual SAR monitoring scenario: a) geographic location and footprints of the Sentinel-1 acquisitions for ascending (Track 44) and descending (Track 124) orbits; b) the main active geological features (locations of the main villages are also reported); c) locations of the two GB-SAR systems installed on the northern edge of the Sciara del Fuoco at 190 m a.s.l and 400 m a.s.l., respectively.

(Antonello et al., 2004; Monserrat et al., 2014), has also proved to be a very powerful tool for measuring ground displacements. It has extensively been applied in the monitoring of landslides (Frodella et al., 2018), glacier movements (Dematteis et al., 2017) and volcanic deformations (Calvari et al., 2016), due to its flexibility in observation direction and very high sampling frequency. Indeed, depending on their orientation, GB-SAR devices can detect displacements along directions that are usually blind to space-borne SAR (e.g. North-South).

Moreover, GB-SARs may allow the operator to choose the optimal instrument location (i.e. distance, incidence and azimuth angles), thus permitting to estimate the ground displacement measurements with high spatial resolution, whereas the very high temporal sampling rate allows for continuous measurements, pushing the InSAR technology from "mapping and monitoring" to "surveillance and early warning" (Carlà et al., 2016a, 2016b). GB-SAR has been used for the contemporary identification of volcano slope instability (Di Traglia et al., 2014a) and pressurization of the magmatic/hydrothermal system before eruptive events (Di Traglia et al., 2015; Kuraoka et al., 2018; Calvari et al., 2020). However, the GB-SAR installation, in particular in volcanic contexts, is constrained by the site characteristics (accessibility, hazard, etc.); moreover, its footprint extension is clearly much more limited with respect to that of space-borne system, thus limiting the size of the sensed area.

In this paper, the integration of measurements deriving from Sentinel-1 (S-1) images acquired over Stromboli Island (Italy) and from those obtained by two GB-SAR systems (Di Traglia et al., 2014a; Schaefer et al., 2019) is presented. S-1 data have been acquired from ascending and descending passes (see Fig. 1) and processed by using the MT-InSAR Small BAseline Subset (SBAS) approach (Berardino et al., 2002; Casu et al., 2014; Manunta et al., 2019). The two GB-SAR are installed at 190 m a.s.l. (GB-SAR NE190) and at 400 m a.s.l. (GB-SAR NE400) (see Fig. 1) on the northern edge of the unstable flank (Sciara del Fuoco; SdF) of Stromboli volcano.

The integration of the information retrieved from the available datasets allowed us to:

1) Reconstruct the 3D deformation field of the SdF following the 2014 flank eruption (Di Traglia et al., 2018c). This has been achieved by jointly exploiting the space-borne and the ground-based data collected between April 2015 and June 2019, through a linear inversion of the MT-InSAR measurements obtained by the two different SAR systems;
2) Study the July–August 2019 eruption (Plank et al., 2019; Turchi et al., 2020) by analysing single interferograms, stacks of interferograms, and coherence maps collected in the sin- and post-eruptive periods.

Both short- and long-term analyses highlight the strong complementarity of the space-borne and ground-based techniques for mapping and monitoring volcano deformation phenomena.

2. Technical background

InSAR is a well-established remote sensing technique that allows detecting and measuring surface deformation over large areas of Earth with centimetre to millimetre accuracy (Gabriel et al., 1989). It exploits the phase difference (interferogram) between two SAR images acquired over the same area at different epochs (temporal baseline) and with different orbital positions (spatial baseline), and provides an estimate of the occurred ground displacement projected along the satellite LOS.

Starting from the beginning of 90's, thanks to the large availability of SAR satellite constellations, the space-borne InSAR technique has extensively been applied to study a large variety of deformation phenomena such as those associated with earthquakes, volcanic activity, slope instability, etc. (Massonnet et al., 1993, 1995; Peltzer and Rosen, 1995; Rignot, 1998; Tesauro et al., 2000). Since then, the interest of the scientific community has progressively moved from the investigation of a single deformation event toward the study of the temporal evolution of the detected LOS-projected displacements by simultaneously exploiting the information available from sequences of InSAR interferograms. In this sense, a first attempt has been represented by the stacking techniques (Fialko and Simons, 2001; Peltzer et al., 2001; Fialko, 2004) that compute the LOS mean deformation velocity by adding the unwrapped interferometric phase from individual pairs, converting the summed phase to the LOS displacements, and dividing the latter by the total cumulative time span of all interferometric pairs in the stack. In this way, the stacking techniques allow getting an estimate of the mean deformation rate of the investigated area (improved with respect to the one obtained by considering a single interferometric pair) by reducing the atmospheric and/or orbital artefacts.

However, it has been with the development of the so-called MT-InSAR techniques (Ferretti et al., 2001; Berardino et al., 2002; Lanari et al., 2004a; Werner et al., 2003; Hooper, 2008) that it has been possible to get further useful information on both the spatial distribution and the temporal evolution of the detected LOS-projected displacements. Indeed, these techniques, managing large sequences of SAR acquisitions and of the related differential interferograms, selected according to different strategies, generate deformation time-series and corresponding velocity maps for each coherent pixel of the investigated scene.

Among them, we focus on the one referred to as Small BAseline Subset, SBAS (Berardino et al., 2002) that relies on an appropriate combination of differential interferograms produced by data pairs characterized by small temporal and spatial baselines in order to limit decorrelation effects (Zebker and Villasenor, 1992). Over times, this approach has successfully been exploited for the investigation of different scenarios, such as volcanoes, tectonics, landslides, and anthropogenic-induced land motions (Bonano et al., 2016; Calò et al., 2014; Casu et al., 2006; D'Auria et al., 2015; Lanari et al., 2004b, 2007a, 2007b, 2010; Manzo et al., 2012; Sansosti et al., 2010; Scifoni et al., 2016; Zeni et al., 2011); moreover, it has demonstrated that it can generate deformation time-series and relative mean deformation velocity maps with accuracies of about 5–10 mm and 1–2 mm/year, respectively (Casu et al., 2006; Manunta et al., 2019). Very recently, a parallel version of the SBAS algorithm, referred to as P-SBAS (Casu et al., 2014; Zinno et al., 2015, 2017), that permits to generate in an automatic and unsupervised way advanced InSAR products by taking full benefit from parallel computing architectures (such as cluster, grid and cloud computing infrastructures), has been developed. This approach can efficiently deal with large amounts of SAR data acquired from different sensors (such as those collected from the ERS-1/2 and ENVISAT systems as well as from the COSMO-SkyMed and TerraSAR-X ones). Moreover, the P-SBAS approach has further been modified to also process the SAR data collected by the S-1 constellation of the European Copernicus Programme. In this case, P-SBAS can take advantage from the data acquisition characteristics of the S-1 Interferometric Wide swath (IW) mode in terms of parallelization strategy (Zinno et al., 2018; Manunta et al., 2019; Lanari et al., 2020).

The S-1 constellation is made up of two twin satellites operating at C-band, collects images over land with a wide spatial coverage and a short revisit time (down to 6 days in the case of the two operating satellites are both available). Moreover, the S-1 images are provided to users via a free and open access data policy. These characteristics have allowed, for the first time in the SAR satellite scenario, the migration from back analysis to the development of operative monitoring services. Furthermore, they have fostered the investigation of Earth surface deformation phenomena at unprecedented spatial scale and with a high temporal rate, thus encouraging, apart from the generation of LOS-projected deformation time-series, the retrieval of Vertical and East-West component deformation time-series. However, some limitations of the space-borne systems still exist. First, the satellite revisit time, although progressively reduced with respect to the earlier SAR systems, does not allow

following fast and very-short-term (with respect to the satellite revisit time) deformation phenomena. Secondly, the (nearly) polar direction of the sensor orbits prevents the retrieval of the North-South deformation components with the same accuracy obtained from the vertical and East-West ones.

Accordingly, the exploitation of ground-based SAR systems can be a complementary solution to the satellite systems. As for the satellite scenario, the GB-SAR devices are remote sensing imaging systems (Rudolf et al., 1999; Antonello et al., 2004; Monserrat et al., 2014) that emit and receive a burst of microwave pulses, repeating this operation while the sensor is moving (Rudolf et al., 1999). In this case, the SAR technology is made possible by moving the real antennas along a rail (track), and the length of this rail determines the cross-range resolution of the acquired images (Antonello et al., 2004). The GB-SAR measures the amplitude and the phase of the received radar signal. By using interferometric techniques, we can exploit the phase difference between the GB-SAR acquisitions to derive information on deformation of the observed scene (as for space-borne measurements). However, displacements, even in the best installation conditions, remain measured along the LOS. This can be very limiting for the unstable volcano flanks because: i) they are very large and can have large variability of inclination and orientation, and ii) displacements can be related both to gravitational phenomena (along the slope vectors) and to volcanic phenomena such as inflation/deflations and/or cooling of lava/pyroclastic material (see Di Traglia et al., 2018a, 2018b).

On the other hand, it is possible to take advantage from the peculiarity of space-borne and ground-based systems to overcome the above-mentioned limitations, through a joint exploitation of these independent displacement measurements (e.g. Bardi et al., 2016). The complementary use of the satellite and terrestrial techniques allows us to have, at the same time, the mapping of phenomena on a large scale (satellite), and the ability to follow, and sometimes to anticipate, fast phenomena (terrestrial). In addition, where possible, the inversion of the deformation measurements retrieved by the two different techniques permit to reconstruct the 3D displacement field.

3. The Stromboli volcano

The 916 m-high Stromboli Island (Fig. 1b) is the emerged portion of a ~ 3000 m-high volcano located in the Tyrrhenian Sea, off the southern coast of Italy (Francalanci et al., 2013). Stromboli volcano is affected by bi-lateral instability which formed two scars, one on its NW flank (SdF depression) and the other one on the SE flank (Le Schicciole – Rina Grande depression) (Kokelaar and Romagnoli, 1995; Tibaldi, 2001; Romagnoli et al., 2009; Francalanci et al., 2013; Risica et al., 2019). The SdF depression is a landslide scar that extends down to 700 m below sea level on the NW flank of the volcano, with slopes ranging from 40° to 45° in the subaerial part, and decrease in the underwater part, remaining >30° up to 300–400 b.s.l.. SdF is partially filled with volcaniclastic deposits and lavas (Casalbore et al., 2010, 2011; Di Traglia et al., 2018b,

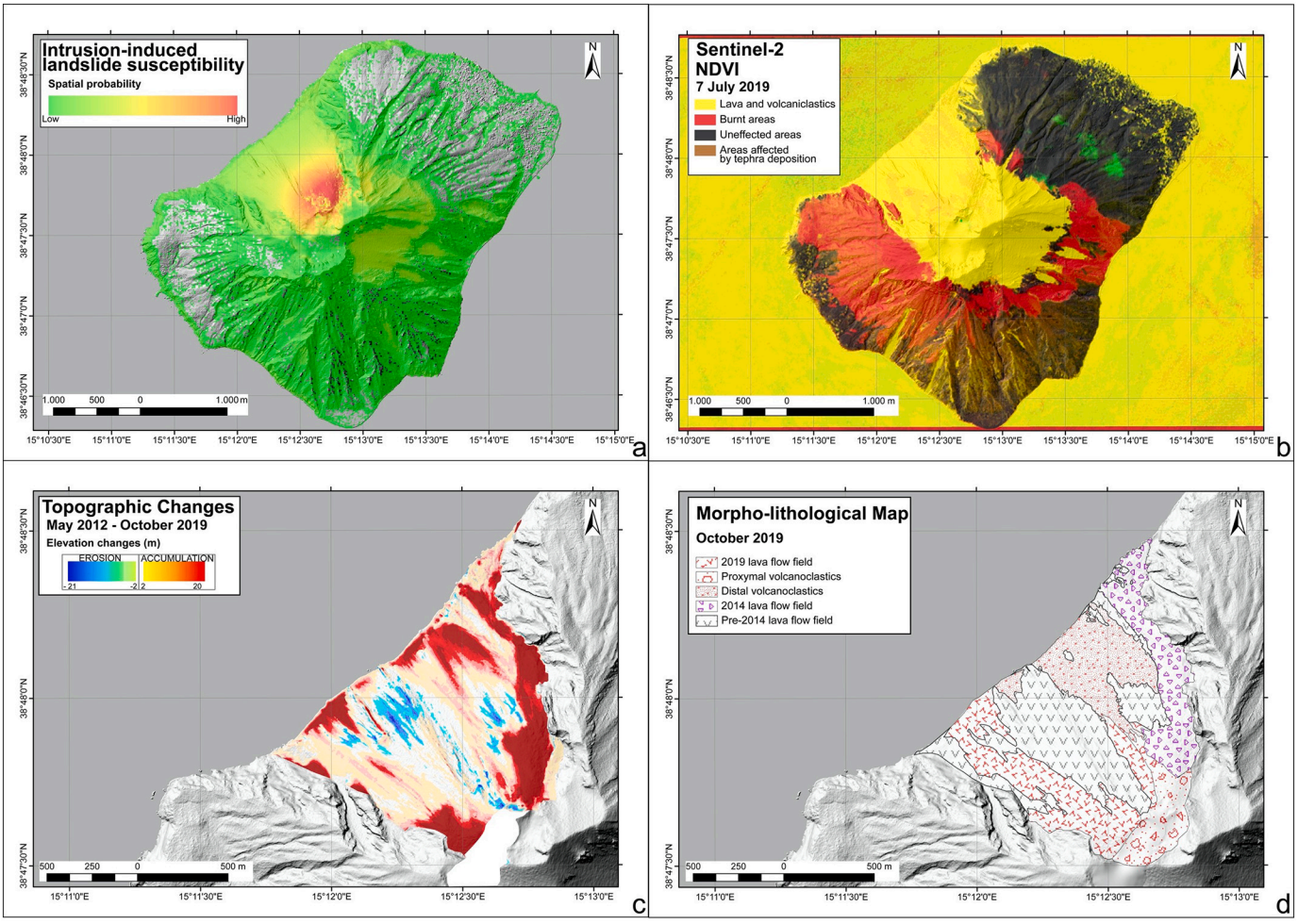

Fig. 2. The Stromboli Island scenario maps. a) Intrusion-induced landslides susceptibility map (based on Di Traglia et al., 2018d); b) Normalized Difference Vegetation Index applied on Sentinel-2 image collected on 7th July 2019, highlighting the area affected by tephra deposition and wildfire damage after the 3rd July 2019 paroxysmal explosion; c) topographic change detection map, highlighting the elevation variation in the Sciara del Fuoco area between May 2012 and October 2019 (modified after Di Traglia et al., 2020); d) morpho-lithological map of the Sciara del Fuoco area, after the July–August 2019 eruption.

Table 1
Eruptive activity and slope processes between November 2014 and November 2019.

Period	Eruptive activity	Slope processes	References
Nov 2014 – Sep 2016		Erosion of the 2014 lava field; rockfall and gravel flows along the SdF	Di Traglia et al. (2018a)
26th Jul 2017	Major explosion		Giudicepietro et al. (2019), Bevilacqua et al. (2020)
23th Oct 2017	Major explosion		Giudicepietro et al. (2019), Bevilacqua et al. (2020)
1st Nov 2017	Major explosion		Giudicepietro et al. (2019), Bevilacqua et al. (2020)
1st Dec 2017	Major explosion		Giudicepietro et al. (2019), Bevilacqua et al. (2020)
Dec 2017 – Jan 2018	Intense spatter activity and a lava overflow	Frequent rockfall and gravel flows during spatter activity	Schaefer et al. (2019), Giudicepietro et al. (2019)
7th Mar 2018	Major explosion		Giudicepietro et al. (2019), Bevilacqua et al. (2020)
18th Mar 2018	Major explosion		Giudicepietro et al. (2019), Bevilacqua et al. (2020)
24th Apr 2018	Major explosion		Giudicepietro et al. (2019), Bevilacqua et al. (2020)
26th Apr 2018	Major explosion		Giudicepietro et al. (2019), Bevilacqua et al. (2020)
Dec 2018 – Jan 2019	Intense spatter activity	Frequent rockfall and gravel flows during spatter activity	Schaefer et al. (2019), Giudicepietro et al. (2019)
3rd Jul 2019	Paroxysmal explosion		Giudicepietro et al. (2020)
3rd Jul 2019 – 30th Aug 2019	Lava flow from the SW crater rim and occasionally from the NE crater	Frequent rockfall and gravel flows during effusive activity	Plank et al. (2019)
28th Aug 2019	Paroxysmal explosion		Giudicepietro et al. (2020)
29th Aug 2019	Major explosion		Giudicepietro et al. (2020)
Sep 2019–Nov 2019	Frequent Strombolian explosion	Frequent rockfall and gravel flows	This study

2020) emitted from the summit crater terrace and from ephemeral vents located within the SdF (Di Traglia et al., 2018d). Slope instability phenomena at Stromboli are classified, on the base of their size and movement, into three types (Di Traglia et al., 2018d; Schaefer et al., 2019): 1) "deep-seated gravitational slope deformations" evolving to "rock or debris avalanches" from the SdF (volumes $>10^6$ m^3); 2) "rock (rotational or planar) slides" evolving to "rock avalanches" from the SdF (volumes$\approx 10^6$ m^3); 3) "rock falls" or "gravel/debris slides" evolving to "gravel/debris flows" (volumes $\approx 10^5$ m^3).

Stromboli is one of the most well-known volcanos in the world and its persistent activity, consisting of frequent, small scale, explosions, gives its name to *Strombolian activity* (Blackburn et al., 1976). The most hazardous phenomena at Stromboli Island are the mass-flows induced tsunamis (Nave et al., 2010; Fornaciai et al., 2019), likely generated both by intrusion-related landslides from the SdF (Fig. 2a) or by the entry into the sea of pyroclastic density currents (PDCs) produced during high-intensity explosions (locally called "major" or "paroxysmal"; Barberi et al., 1993). Tsunamis also occurred in recent times as in 1879, 1916, 1919, 1930, 1944, 1954, 2002, and 2019, accounting for an average of 1 tsunami every 20 years (Maramai et al., 2005). Tsunamis can affect large areas both on the coast of Stromboli Island and on the coasts of the other Aeolian islands and the Tyrrhenian coasts of southern Italy (Fornaciai et al., 2019).

The distinctive persistent Strombolian activity is characterized by intermittent explosions from three vent areas (NE, SW and Central) in a summit crater terrace, located at ≈ 750 m a.s.l. in the upper part of the SdF (Calvari et al., 2014). This activity, showing intensity and frequency fluctuations over time, is often punctuated by lava overflows from the crater terrace (Calvari et al., 2014), by flank eruptions, with the outpouring of lava flows from ephemeral vents (Marsella et al., 2012; Di Traglia et al., 2020), or by high-intensity explosions, that can have a severe impact on the island, as occurred during the 2019 eruption (Fig. 2b). Moreover, recent flank eruptions occurred in 2007 and 2014 (Di Traglia et al., 2014a, 2018c). The 2007 eruption began on 27th February 2007 with the opening of a first ephemeral vent at 650 m a.s.l. at the base of the NE crater area, which was followed by the opening of a second ephemeral vent at 400 m a.s.l. within the SdF (Marsella et al., 2012; Di Traglia et al., 2014a). After the 2007 flank eruption, Stromboli had periods of higher than ordinary activity in September 2008, May 2009, July–September 2011, December 2012–March 2013, with more intense and frequent explosions, some overflows, spattering, and, sporadically, some major explosions (Calvari et al., 2014; Di Traglia et al., 2014a, 2014b). After these events, Stromboli experienced a period of intense and frequent explosions, together with overflows, spattering,

and frequent landslides from the crater terrace since late May 2014, that culminated on 7th August 2014 with the onset of the 2014 flank eruption (Di Traglia et al., 2015, 2018a, 2018b, 2018c). The effusion lasted until 13th November 2014 (Di Traglia et al., 2018a, 2018c), with the emplacement of 2.697 ± 0.190× 10^6 m^3 of lava on the SdF from a fracture located at 650 m a.s.l. (Fig. 2c; Di Traglia et al., 2018c, 2020). After the 2014 flank eruption, Stromboli was characterized by very low eruptive activity in 2015 and 2016 (Table 1), when strong erosion of the subaerial SdF occurred (Di Traglia et al., 2018a, 2020). Afterward, Stromboli had periods of higher than ordinary activity in July 2017, October 2017–January 2018, March–April 2018, December 2018–January 2019, with more intense and frequent explosions, some overflows, spattering, and, some major explosions (Giudicepietro et al., 2019; Inguaggiato et al., 2019; Bevilacqua et al., 2020; Table 1).

On 3rd July 2019, Stromboli experienced a paroxysmal explosion (14:45 UTC; Giudicepietro et al., 2020; Inguaggiato et al., 2020; Calvari et al., 2021), causing a casualty and inducing a wide-spread wildfire (Turchi et al., 2020; Fig. 2b), generating an eruptive plume up to 4–5 km (Plank et al., 2019; Métrich et al., 2021) and a PDC flowing along the SdF that induced a small tsunami wave (Fornaciai et al., 2019; Giordano and De Astis, 2021). In the following months, lava outpoured from a vent localized in the SW crater, and sporadically from the NE one (Fig. 2d). On 28th August 2019, a new paroxysmal explosion occurred (Turchi et al., 2020; 10:27 UTC; Inguaggiato et al., 2020), and a new PDC flowed along the SdF, generating another small tsunami wave (Fornaciai et al., 2019). This second explosion was followed by strong volcanic activity, culminating with a lava flow emitted from the SW-Central crater area (in the night between 29th and 30th August 2019). Coarse-grained tephra (spatter bombs and ballistic blocks), erupted during the 3rd July 2019 and 28th August 2019 paroxysms, have been mainly accumulated on the summit of the island (Fig. 2d).

In particular, the 3rd July 2019 tephra fallout (lapilli and ash) has impacted the south-western and southern part of the island, including the village of Ginostra (Turchi et al., 2020), whereas the 28th August 2019 tephra fallout has affected only a small part of the island, being its dispersal axis easterly directed. Subsequently, the eruptive activity decreased, although frequent instability phenomena linked to the growth of new cones on the edge of the crater terrace occurred.

4. Space-borne and ground-based SAR data

We investigate the recent Stromboli deformation history starting from 2015 up to the end of 2019 with different space-borne and ground-based data availability. According to the volcano behavior and the paroxysm of July–August 2019 eruption, we divide the investigation (and the data) into pre-, sin- and post-eruptive periods.

For the satellite InSAR analysis, we exploited the archive of Sentinel-1 SAR data acquired over Stromboli spanning the 24th April 2015 – 5th November 2019 time interval. In particular, we considered 221 and 226 SAR data collected from ascending (Track 44) and descending (Track 124) orbits, respectively. Overall, we generated 561 ascending and 606 descending differential interferograms, respectively. To this aim, we used the 1-arcsec Shuttle Radar Topography Mission (SRTM) Digital Elevation Model (DEM) of the volcano to remove the topography related phase components and then we applied a complex multilook operation with 5 looks in the range direction and 1 look in the azimuth one.

The final results have been resampled on the DEM grid, thus obtaining a final pixel size of about 30 m × 30 m. In Table 2 we report the main characteristics of the considered SAR data-sets. We performed the satellite InSAR processing according to the following three time periods: 1) 24th April 2015 - 26th June 2019, being the pre-eruptive period; 2) 2nd July 2019 – 25th August 2019, representing the sin-eruptive period; 3) 31st August 2019 – 5th November 2019, corresponding to the post-eruptive period.

For each period, we adopted different processing strategies in order to take into account the 2019 eruptive behavior comprising the occurred two paroxysmal explosions and lava effusion. In particular, for the pre-eruptive period, since no preparatory phase occurred, we applied to the ascending and descending SAR data-sets the P-SBAS technique (Casu et al., 2014; Manunta et al., 2019) to automatically generate displacement time-series and the corresponding mean deformation velocity maps. Moreover, by benefiting from the availability of the ascending and descending acquisition geometries, we were able to discriminate the Vertical and East-West components (Casu and Manconi, 2016; De Luca et al., 2017) of the computed displacements for the pixels common to the orbits results.

For the sin-eruptive period, we observed a high level of decorrelation noise within the interferometric phase signal due to the deposits of the material emitted during the 3rd July 2019 paroxysm, which changed the scene from the electromagnetic point of view. This effect was particularly evident in the central-southern sector of the SdF, thus making the deformation time-series analysis not reliable. On the contrary, this sector could be investigated by considering differential interferograms and the corresponding spatial coherences computed with the SAR data acquired within this time interval.

Finally, for the post-eruptive period, we noted a decrease of the decorrelation noise within the computed differential interferograms in the Southern sector of the SdF and detected a clear displacement signal. Accordingly, we exploited a specific redundant interferogram network for both ascending and descending orbits that we used to generate the relative mean deformation velocity maps by applying the InSAR stacking technique mentioned in Section 2 (Fialko and Simons, 2001). In particular, to maximize the signal/noise ratio and emphasize the time-persistent signals we applied the following approach: i) we computed and unwrapped interferograms with a 6 days temporal span in order to preserve the coherence of the scene and reduce the Phase Unwrapping errors; ii) we referred each displacement map (derived from each considered interferogram) to the same stable point located in an area as close as possible to the SdF; iii) finally, we averaged all the computed displacement maps dividing them by their respective time span, thus obtaining the mean deformation velocity map of the area. With this

Table 2
Main characteristics of the exploited Sentinel-1 SAR dataset.

	Ascending orbits	Descending orbits
Wavelength	5.5 cm	
Acquisition mode	TOPS	
Look angle	38.14° – 38.84°	37.33° – 37.61°
Heading angle	~348°	~192°
Spatial resolution	~30 m × 30 m	
Track	44	124
Time interval	30/04/2015–24/10/2019	24/04/2015–05/11/2019
Number of SAR acquisitions	221	226
Acquisition time	16:55 UTC	05:05 UTC

Table 3
Number of Sentinel-1 SAR images used for the analysis of the investigated three periods.

	Ascending orbits	Descending orbits
April 2015 – June 2019	205	201
3rd July 2019 – 30th August 2019	9	10
31st August 2019 – 5th November 2019	12	10

stacking approach we tried to limit the impact of the atmospheric artefacts and emphasize the displacement signals. We estimated the stacking noise level by considering the standard deviation of the signal outside the SdF, where we assume no significant deformation is present.

Moreover, as for the pre-eruptive period analysis, by benefiting from the two acquisition orbits, we discriminated the Vertical and East-West deformation components.

In Table 3 we report the number of ascending and descending SAR images for each identified period.

For what concerns the GB-SAR systems at Stromboli, we remark that they exploit a 4 m long rail along which the transmitting and receiving antenna move. The recorded signals measure ground displacements along the radar LOS, through the InSAR technique applied to the phase differences between the backscattered signals associated with two consecutive SAR images (Antonello et al., 2004; Di Traglia et al., 2015). In particular, the interferograms are obtained from phase information of "averaged" images, in the sense that they are created by averaging the phase information derived from the different acquisitions. Specifically, the images are averaged every half hour, which means that 3 images are exploited for the GB-SAR NE400 system and 15 for the GB-SAR NE190 one. After a resampling operation, the pixel size is of about 2 m by 2 m along both range and cross range (Casagli et al., 2009). Displacement cumulated maps are calculated using a staking algorithm to sum, pixel by pixel, the displacements for every consecutive pair of images, whereas displacement time series of selected points (averaged over 10 pixels) are obtained from cumulative displacement maps with a precision in the displacement measurement of 0.5 mm (Antonello et al., 2004; Di Traglia et al., 2015).

The ability of GB-InSAR to measure volcano deformation depends, as for all radar system working in interferometric mode, on the persistence of the backscattering and phase coherence over time (for GB-InSAR coherence definition see Antonello et al., 2004). Changes of the target backscattering and the coherence loss are primarily due to significant volcanic phenomena (e.g. lava flows or rock avalanches; Di Traglia et al., 2018b). A coherence threshold equal to or above 0.7 is required to recognize deformation areas from a GB-InSAR interferogram, whereas a threshold of 0.5 is set during the interferograms stacking operation. Moreover, a threshold on the squared image amplitude (Calvari et al., 2016, 2020) of the backscattering image has been set for both radars at 55 dB. Due to the position of the two systems the LOS of both GB-SAR devices are mostly sensitive to the N-S horizontal component of occurred displacements (average azimuth angle = 15°). Accordingly, the negative and positive values of the displacements indicate a movement toward and away from the sensor, respectively. We further remark that the two GB-SAR devices, located in a stable area N of the SdF, are used to monitor the NE portion of the summit crater terrace and the northern portion of the SdF (Schaefer et al., 2019), being the area most affected by vent opening and intrusion-related landslides in recent eruptions (Di Traglia et al., 2018d). The features of the two GB-SAR devices are reported in Table 4.

Table 4
Technical features of the two GB-SAR devices installed at Stromboli volcano.

System	GB-InSAR NE400[a]	GB-InSAR NE190[b]
Model	GB-InSAR LiSAmobile k09	GB-InSAR LiSAmobile k09
Band	Ku	Ku
Revisiting time [min]	11 (until Nov. 2017) 6 (since Nov. 2017)	2
Averaging interval [min]	33	30
Look Angle [deg]	63.8° – 90.0°	65.0° – 113.5°
Heading Angle [deg]	143° – 217°	115° – 245°

From [a]Di Traglia et al. (2015) and [b]Schaefer et al. (2019).

5. Multi-geometry InSAR measurements fusion

To take benefit from the availability of different space-borne and ground-based data sets, the obtained InSAR measurements must be properly merged according to their respective acquisition geometry. Here-below the data geometry characteristics and the adopted fusion strategies are described.

The acquisition geometry of the SAR satellite sensors is essentially defined by Fig. 3a, b, where the look angle θ is the angle between the nadir and the radar LOS, and the satellite heading angle α represents the angle between the North direction and the projection of the sensor path on the ground. Presently, the available SAR satellites follow nearly polar orbits, implying values of α around 345° for ascending satellite passes and around 195° for descending ones. The look angle for each pixel on the ground, instead, is strongly satellite dependent varying on the image footprint extent (swath) and on the image acquisition mode. For the Sentinel-1 Interferometric Wide Swath mode, the look angle between near- and far-range varies from ~29° to ~46° (ESA. Sentinel-1 SAR User Guide—Interferometric Wide Swath. 2018. https://sentinels.copernicus.eu/web/sentinel/user-guides/sentinel-1-sar/acquisition-modes/interferometric-wide-swath).

As already said, the displacement values detected by both space-borne and ground-based InSAR are one-dimensional measurements that derive from the projection, along the radar LOS, of vertical, east and north displacement components (d_U, d_E, d_N) (Elachi, 1988; Curlander and McDonough, 1991). In the following we describe the surface motions in terms of displacement rate, although the same description holds for discrete displacements. In this respect, the LOS velocity v_{LOS} can be expressed as follows:

$$v_{LOS} = (cos\theta - sin\theta cos\alpha \;\; sin\theta sin\alpha) \begin{pmatrix} v_U \\ v_E \\ v_N \end{pmatrix} \quad (1)$$

where v_U, v_E and v_N are the vertical, east and north displacement rates, respectively. In the previous equation the strong limitation of the satellite SAR technology becomes clear, which, due to the polar orbit, is not very sensitive to the displacement component along the north direction being $sin\alpha$ very close to zero.

By referring to Eq. (1), to retrieve the three motion components, at least three non-coplanar LOS vectors are needed (Rocca, 2003). To this aim, and as described in the previous paragraph, we exploit the InSAR measurements retrieved from one ascending and one descending P-SBAS S-1 processing and, as third equation, from one of the two available GB-SAR systems, which results to be necessary to retrieve an accurate reconstruction of the 3D displacement field. It is important noting that the estimation of the vertical, east and north deformation components is only possible on the common area imaged by all the exploited observation systems. Accordingly, to maximize the above-mentioned common area it is more convenient to exploit the GB-SAR NE190 only, which illuminates a large part of the SdF, while the GB-SAR NE400 just senses the summit part of Stromboli volcano thus strongly limiting the reconstruction of the 3D field.

Moreover, we highlight that the GB-SAR systems located at Stromboli volcano mostly illuminate along the North-South direction, thus guaranteeing a high sensitivity in the estimation of the deformation component in the same direction. As for the SAR satellite sensors, the acquisition geometry of the GB-SAR systems is essentially defined by Fig. 3c, d, where the look angle θ and the heading angle α have the same definition as for the satellite case described at the beginning of this section; moreover, the specific values are reported in Table 4.

To perform the multi-geometry InSAR measurements combination, we first averaged the GB-SAR displacement maps to make the results comparable (in terms of ground resolution) with the P-SBAS S-1 ones. Secondly, we selected the SRTM-1 arcsec as the common grid to refer both satellite and ground based SAR analysis. The grid alignment was

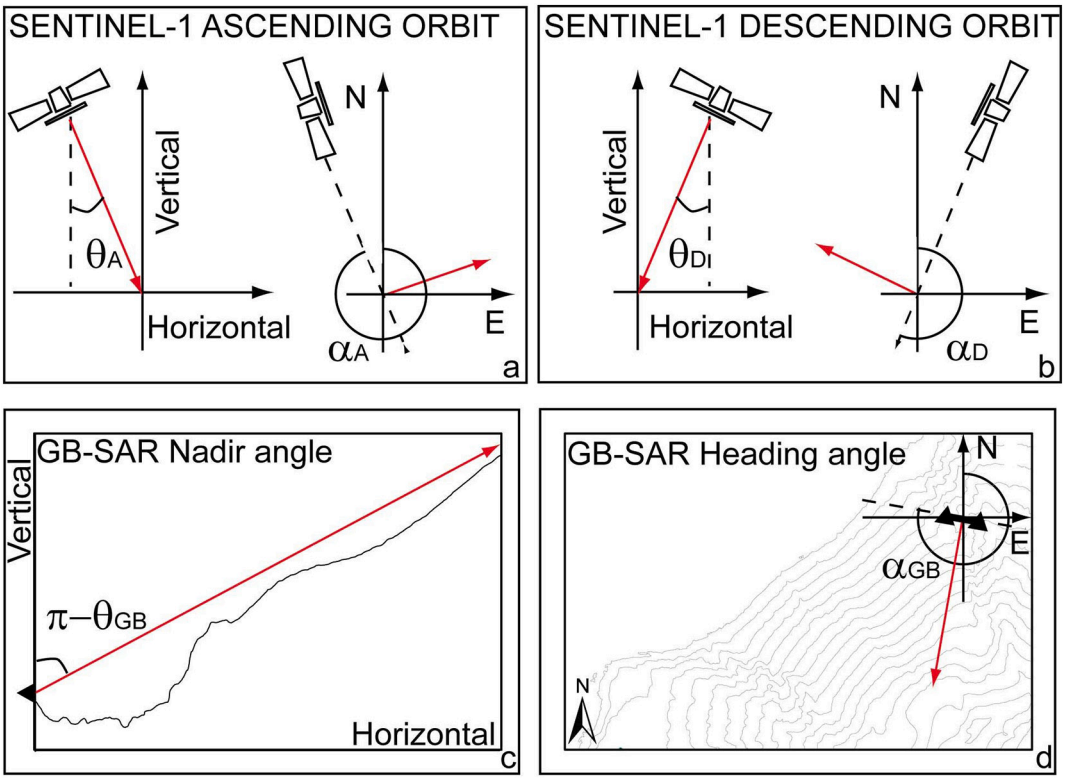

Fig. 3. SAR reference geometries. a) Sentinel-1 ascending orbit. b) Sentinel-1 descending orbit, c-d) GB-SAR system. θ: look angle; α: heading angle.

performed following a nearest neighbourhood approach. Finally, among all ground points (pixels) covering the SdF area, we selected those that were common to both satellite and GB-SAR displacement maps.

According to De Luca et al. (2017) and Casu and Manconi (2016), the system of equations to solve for each common pixel is the following:

$$\begin{cases} v_{losA} = v_U cos\theta_A - v_E sin\theta_A cos\alpha_A - v_N sin\theta_A sin\alpha_A \\ v_{losD} = v_U cos\theta_D - v_E sin\theta_D cos\alpha_D - v_N sin\theta_D sin\alpha_D \\ v_{losGB} = v_U cos\theta_{GB} - v_E sin\theta_{GB} cos\alpha_{GB} - v_N sin\theta_{GB} sin\alpha_{GB} \end{cases} \quad (2)$$

where v_{losA}, v_{losD} and v_{losGB} are the LOS deformation velocities of the ascending, descending and ground-based acquisition geometry, respectively, which are estimated on the common time span to make the measurements comparable (further details are provided in the supplementary material).

Following the implementation of above-described approach, the results of the multi-geometry data fusion are shown in the next section.

6. Results

The S-1 and GB-SAR datasets used in this work cover the April 2015–November 2019 period and are divided, as said in Section 4, into three different time intervals:

1) April 2015–June 2019, being the intra-eruptive periods, between the 2014 and 2019 eruptions;
2) 3rd July 2019 – 30th August 2019, as the sin-eruptive period;
3) 31st August 2019 – 5th November 2019, representing the post-eruptive period.

The description of the achieved results for each of these periods is now in order.

6.1. April 2015 – June 2019

The April 2015 – June 2019 period permits to perform a long term InSAR analysis of the volcano. In Fig. 4 we show the mean deformation velocity maps obtained through the S-1 data processed with the P-SBAS algorithm. In particular, Fig. 4a and b correspond to the results retrieved along the ascending and descending LOS, respectively, while Fig. 4c and d report the corresponding Vertical (also referred to as Up-Down) and East-West displacement components computed for the pixels common to the observations from the two orbits.

The satellite InSAR analysis highlights deformation patterns mainly located in the northern part of the SdF and coincident with the area covered by the 2014 lava flow field. These results are also confirmed by the ground-based long term InSAR analysis shown in Fig. 5a and b.

Moreover, some areas affected by displacements patterns are observed immediately outside the 2014 lava field, in the area below the SW crater and in the central SdF.

In summary:

- Concerning the 2014 lava flow field, the Up-Down component shown in Fig. 4c, reveals the strong subsidence that characterizes the area at whole, whereas in the East-West displacement map shown in Fig. 4d it is possible to identify differential displacements. In particular, in this case most of the movements are toward the west, while there are localized areas that have an eastward movement.
- The 3D displacement field, retrieved via the multi-geometry data fusion and presented in Fig. 6, confirms the strong subsidence of the 2014 lava flow field (see Fig. 6a). Moreover it permits us to show that the horizontal component follows the slope direction (Fig. 6b), suggesting that there are along slope displacements of the entire 2014 lava field. The different contribution to the overall deformation measured on the 2014 lava flow field has been yet estimated by Schaefer et al. (2019), where the contribution of the lava cooling processes has been estimated using the model proposed by Chaussard (2016), considering the lava thickness measured by Di Traglia et al.

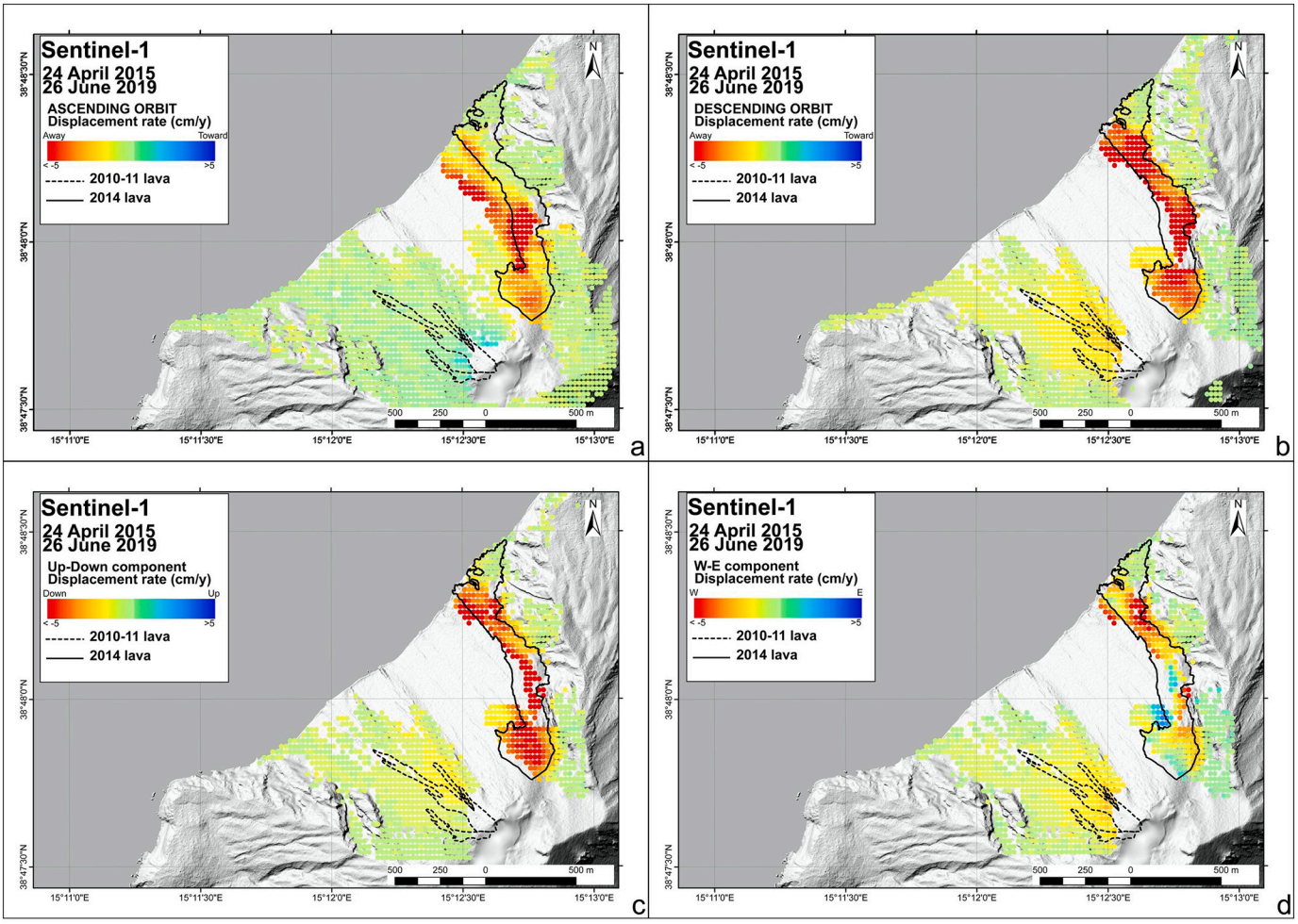

Fig. 4. 24th April 2015 – 26th June 2019 Sentinel-1 displacement. a) Ascending orbit; b) Descending orbit; c) Up-Down component (red dots: subsidence; blue dots: uplift); d) E-W component (red dots: westward displacement; blue dots: eastward displacement). The outline of the 2010–2011 overflows and 2014 lava flow field are also reported (derived from Di Traglia et al., 2020).

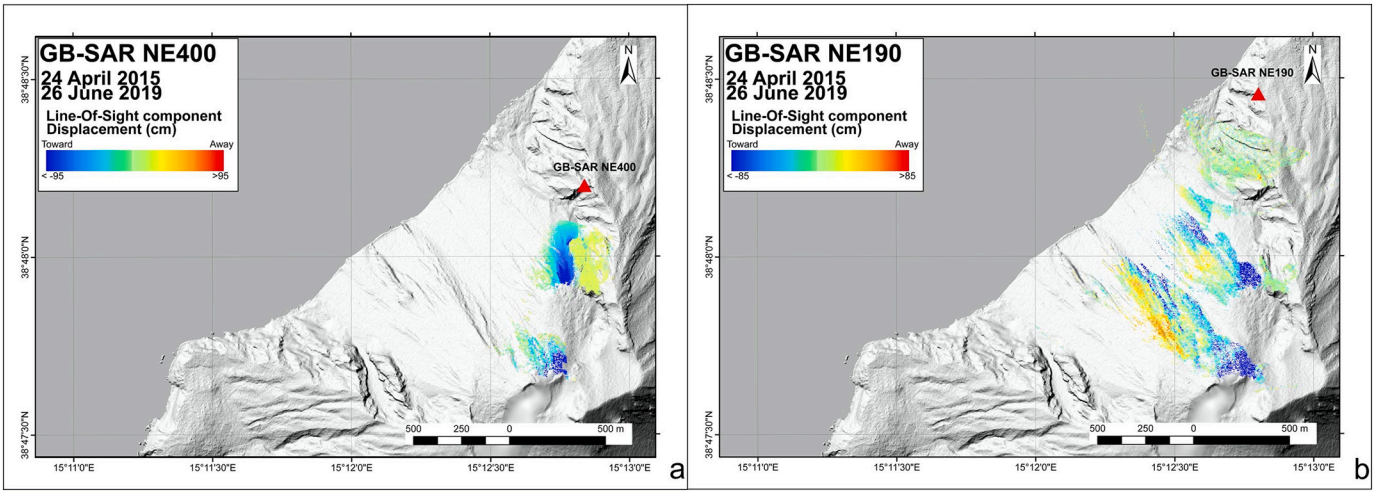

Fig. 5. Pre-eruptive (24th April 2015 – 26th June 2019) cumulated displacement maps based on the a) GB-SAR NE190 and b) GB-SAR NE400 devices, highlighting the displacement related to slope instability in Sciara del Fuoco on the NE crater areas.

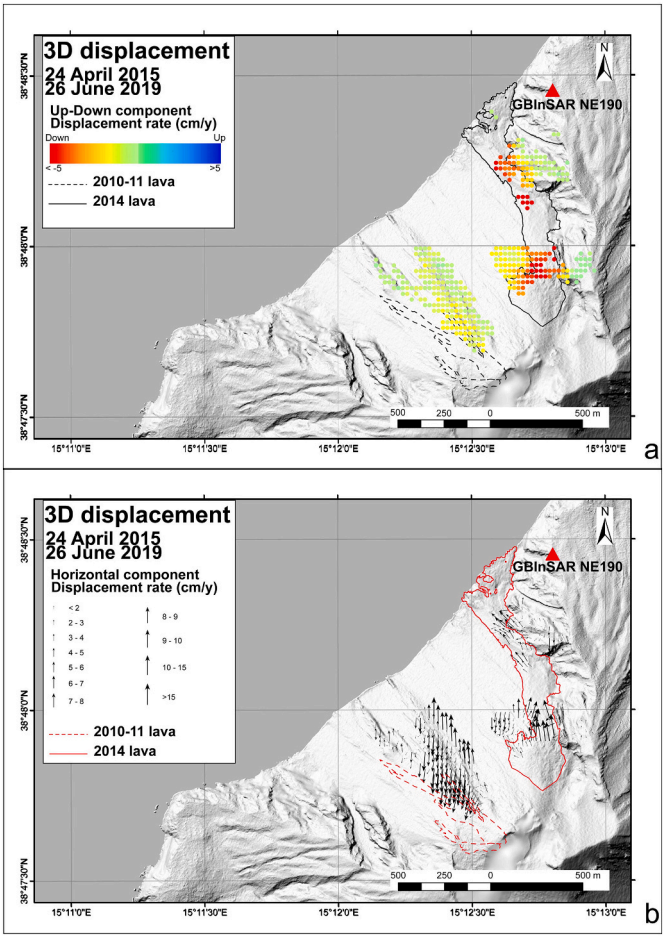

Fig. 6. 24th April 2015 - 26th June 2019 3D displacement, derived from Sentinel-1 and the GB-InSAR NE190 data. a) Up-Down component (red: subsidence; blue: uplift); b) horizontal component (length of the arrows are proportional to the ground displacement according to the legend).

(2018c). The subsidence predicted by the cooling model is then compared to the observed displacement to isolate the remaining contribution. This model predicted ~72% of the observed deformation (110 mm/yr in a 35 m thick flow) in correspondence of the high vertical displacement up-slope in the SdF, whereas in areas characterized by strong horizontal displacement the cooling-induced subsidence predicted by the model (60 mm/yr), accounts for only ~9% of the observed deformation. Schaefer et al. (2019) concluded that the cooling-induced deformation accounts for only a limited part of the rapid flank motion observed after the 2014 Stromboli flank eruption, whereas the maximum observed deformation along the SdF seems more correlated with the slope angle rather than with the lava thickness, suggesting a slope instability control of the observed deformation.

- It is important to note that the coastal area of the lava field, where the lava deltas formed during the 2007 and 2014 eruptions are located, reveals a differential deformation, with a northern stable part and one more localized toward the center of the SdF that shows subsidence (Fig. 6a) and westward movements, indicating a general movement along the slope (Bonaccorso et al., 2009; Di Traglia et al., 2018b).
- Concerning the area below the SW crater, the displacement components derive only from the satellite InSAR analysis and highlight a downwards and westwards deformation pattern (Fig. 4c, d), compatible with movements along the slope.
- In the central SdF area, there are areas characterized by vertical movements in lowering and horizontal southward movements (Fig. 6). These are easily explained by erosion of the material that produces a movement away from both the satellites (vertical downward movement) and from GB-SAR (horizontal movement with a strong southward component). These areas correspond to the eroding areas identified by Di Traglia et al. (2018a) and Di Traglia et al. (2020).
- The Fig. 6 analysis also shows displacements in areas located north and south the 2014 lava flow field. The 3D analysis reveals displacements in the northern edge of SdF, consistent with instability of the local high slopes; while, the southern area has a downward module in the Up-Down component (Fig. 6a), as well as a horizontal component directed toward South (Fig. 6b) consistent with erosion.

We further remark that during the pre-eruptive period from April 2015 to June 2019, the GB-SARs recorded movements toward the sensors in the crater terrace (Fig. 5), with variable displacement rates that mainly increased in December 2017–January 2018 and December 2018–January 2019 (see also Schaefer et al., 2019, and Calvari et al., 2021).

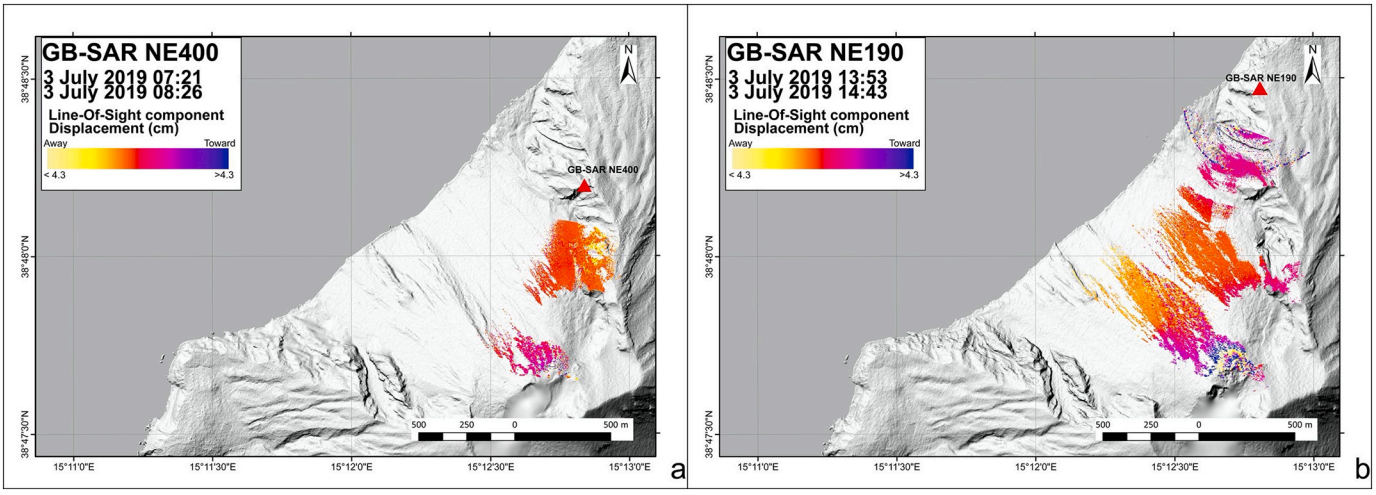

Fig. 7. a) 3rd July 2019 (07:21–08:26 UTC) interferograms generated with GB-SAR NE400 system, testifying the absence of evident deformation hours before the paroxysm; b) 3rd July 2019 (13:53–14:43 UTC) interferograms generated with GB-SAR NE190 system, testifying the strong ground displacement associated with the pre-eruptive inflation.

Table 5
Summary of the ground deformation events recorded during the 2019 eruption by the GB-SAR devices installed at Stromboli.

Start	End	GB-SAR data	Interpretation
3rd July 2019–12:27 UTC	3rd July 2019–14:43 UTC	Rapid increase in the displacement rate toward the sensor in the crater terrace	Strong inflation of the summit area
3rd July 2019–14:43 UTC	3rd July 2019–18:23 UTC	Low coherence	Accumulation and/or rapid movement of newly emplaced material due to paroxysmal explosion
3rd July 2019–18:23 UTC	28th August 2019–10:16 UTC	Variable displacement rate toward the sensor in the crater terrace, with episodes of rapid increase	Episodic inflation of the summit area
28th August 2019–10:16 UTC	28th August 2019–10:49 UTC	Low coherence	Accumulation and/or rapid movement of newly emplaced material due to paroxysmal explosion
29th August 2019–18:37 UTC	29th August 2019–19:42 UTC	Increase in the displacement rate toward the sensor in the crater terrace	Inflation of the summit area
30th August 2019–01:26 UTC	30th August 2019–03:37 UTC	Increase in the displacement rate away from the sensor in the crater terrace	Deflation of the summit area

6.2. 3rd July 2019 – 30th August 2019

On 3th July 2019 Stromboli began a new eruption with a strong paroxysmal explosion, followed by an explosive-effusive phase that lasted 2 months. During this period, the GB-SAR NE190 and NE400 data allowed identifying events of change in the pressurization of the shallow plumbing system, as well as the instability of the newly emplaced material. In particular, Fig. 7 shows the rapid acceleration of deformation, with Fig. 7a testifying the absence of evident deformation several hours before the paroxysm and Fig. 7b highlighting that the eruption was anticipated by a significant ground displacement that started about 2 h before. We underline that the displacement rate reached the peak value of more than 30 mm/h just 2 min before the paroxysmal explosion. Ground deformation was toward the sensors, compatible with a strong and fast inflation of the very shallow storage system (see Di Traglia et al., 2015 for storage system definition). During and soon after the explosions both GB-SAR devices recorded data with low coherence, according to the rapid phenomena associated with the explosion, such as the PDCs that developed along the SdF, and the post-eruptive mobilization of the material emplaced during the explosive activity. In Table 5 the GB-SAR sin-eruptive observations are reported.

On the other side, an interferometric coherence satellite analysis allowed for the identification of the areas impacted by the 3rd July 2019 eruption (Fig. 8). More specifically, in Fig. 8a the coherence map retrieved with two S-1 data acquired before the explosion are shown, whereas in Fig. 8b the one generated with a couple of S-1 images taken across the explosion.

By comparing these two maps, the impact of the paroxysmal event on the electromagnetic properties (and, as consequence, on the coherence signal) of the area that surrounds the crater is strongly evident, which is also correlated with wildfire that affected the Stromboli Island due to the event. Accordingly, the MT-InSAR analysis of ground displacements was not possible due to the observed, abrupt loss of InSAR coherence across the event.

In the following month, the effusive eruption continued, emplacing a lava flow field from the SW crater and small overflows from the NE crater, and ground displacements were variable (Fig. 9a, b). This behavior did not change with the second paroxysm on the 28th August 2019, when no associated deformations were recorded (Fig. 9c and d). However, on the 29th August 2019 a new ground inflation occurred (Fig. 9e), followed, the day after, by a deflation simultaneous with the emission of a last lava flow from the SW crater (Fig. 9f).

6.3. 31st August 2019 – 5th November 2019

The 2019 eruption ended on 30th August 2019, after the emplacement of the lava flow from the SW crater. Following this eruption, an explosive activity remained very significant and the displacements measured by the GB-SAR systems were mainly related to the post-eruptive mobilization of the material emplaced during the explosive activity (Fig. 10). In particular, in Fig. 10a a 1-day interferogram is shown (5th–6th September 2019), highlighting displacements located around the NE crater area, as well as in the SdF, testifying the instability of newly emplaced material. In Fig. 10b, a 6-days interferogram better highlights the slope movements along the SdF (interferometric fringe in the central SdF), whereas in the NE crater area displacements are no

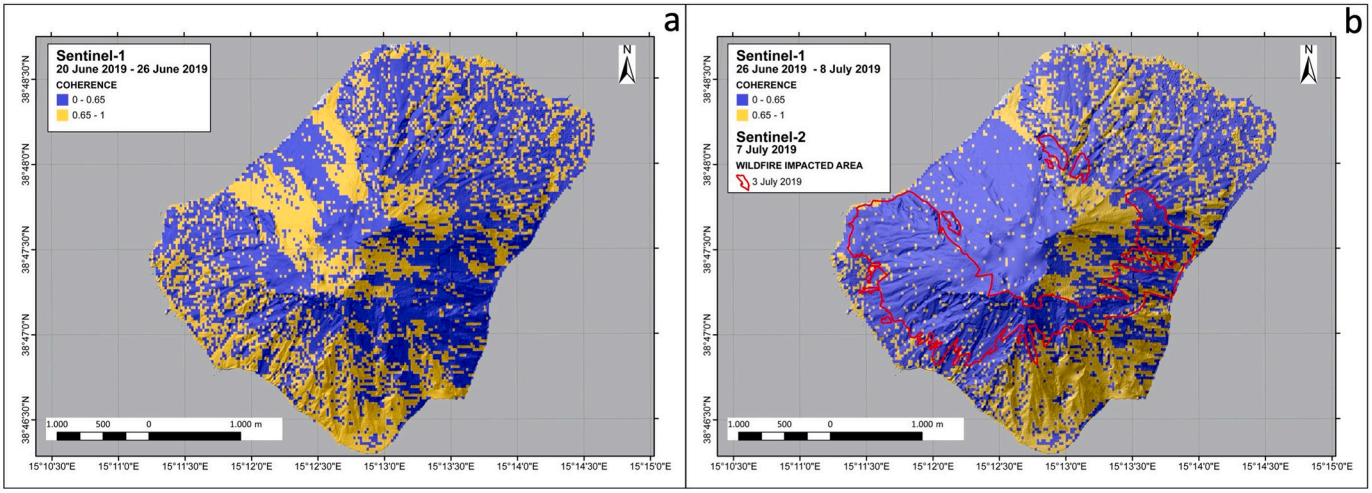

Fig. 8. Sentinel-1 coherence maps: a) before (20th – 26th June 2019) and b) after (26th June – 8th July 2019) the 3rd July 2019 paroxysmal explosion.

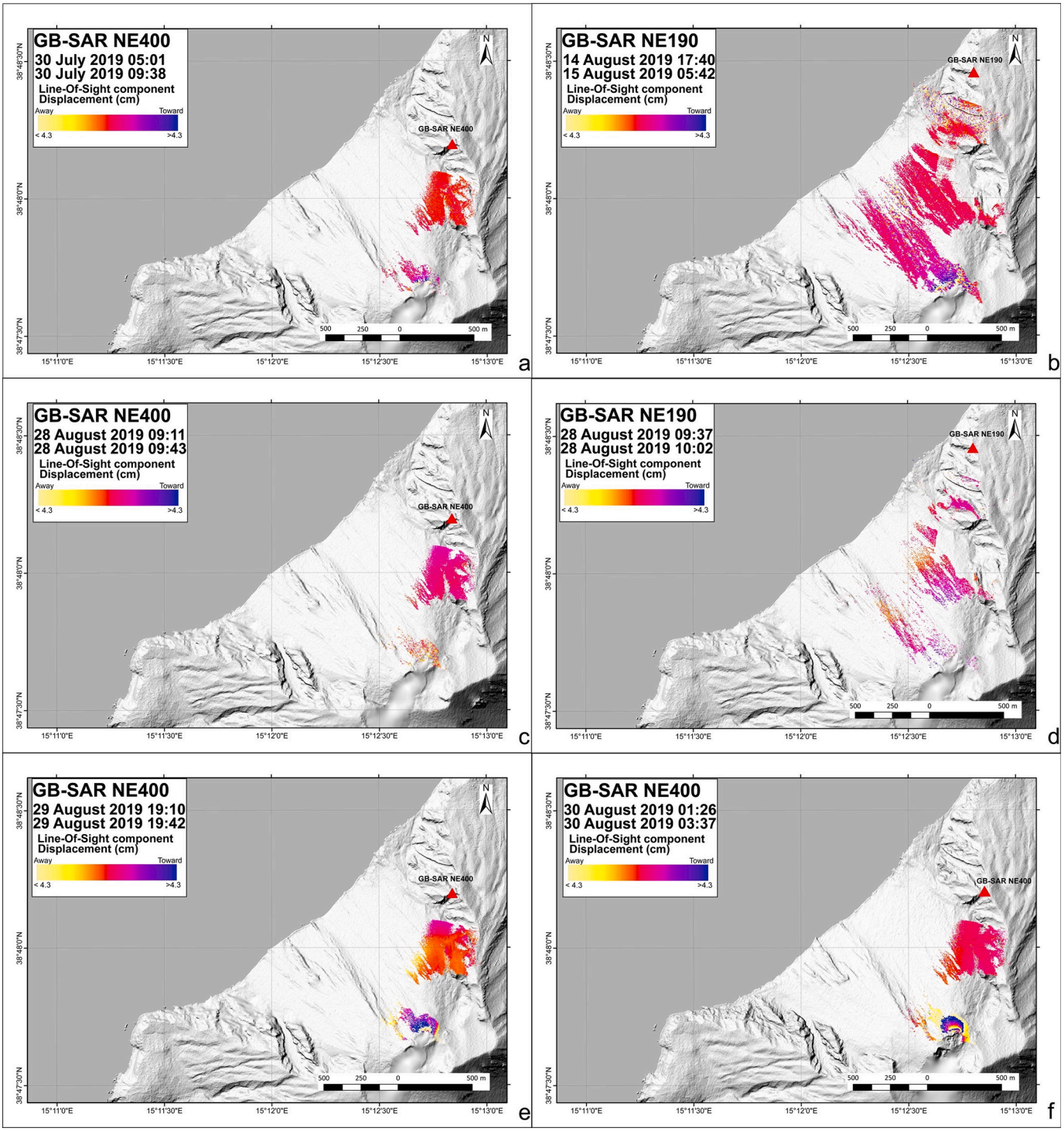

Fig. 9. a) 30th July 2019 (05:01–09:38 UTC) interferogram generated with GB-SAR NE400 system, as example of low displacement rate period during the 2019 eruption; b) 14th July 2019 (17:40 UTC) - 15th July 2019 (05:42 UTC) interferogram generated with GB-SAR NE190 system, testifying increase in displacement rate in the crater terrace within the 2019 eruption; c) 28th August 2019 (09:11–09:43 UTC) interferogram generated with GB-SAR NE400 system, testifying the absence of deformation observed before the 28th August 2019 paroxysm; d) 28th August 2019 (09:37–10:02 UTC) interferogram generated with GB-SAR NE190 system, testifying the low coherence observed before the 28th August 2019 paroxysm; e) 29th August 2019 (19:10–19:42 UTC) interferogram generated with GB-SAR NE400 system, testifying the strong ground displacement before the increase in the effusive activity occurred on 29th–30th August 2019; f) 30th August 2019 (01:26–03:37 UTC) interferogram generated with GB-SAR NE400 system, testifying the strong ground displacement associated with the deflation occurred at the end of the effusive activity. Fig. 9a and b are modified after Calvari et al. (2021).

more detectable due to temporal decorrelation (i.e., too fast movement considering the interferogram interval).

We further remark that ground movements were recorded in the central SdF, but the complete extension of the deformed area could not be measured with the GB-SARs due to the limited extension of the footprint. However, during the post-eruptive period, the satellite InSAR analysis allowed investigating the SdF section not imaged by the GB-SAR, further highlighting the strong complementarity of the satellite

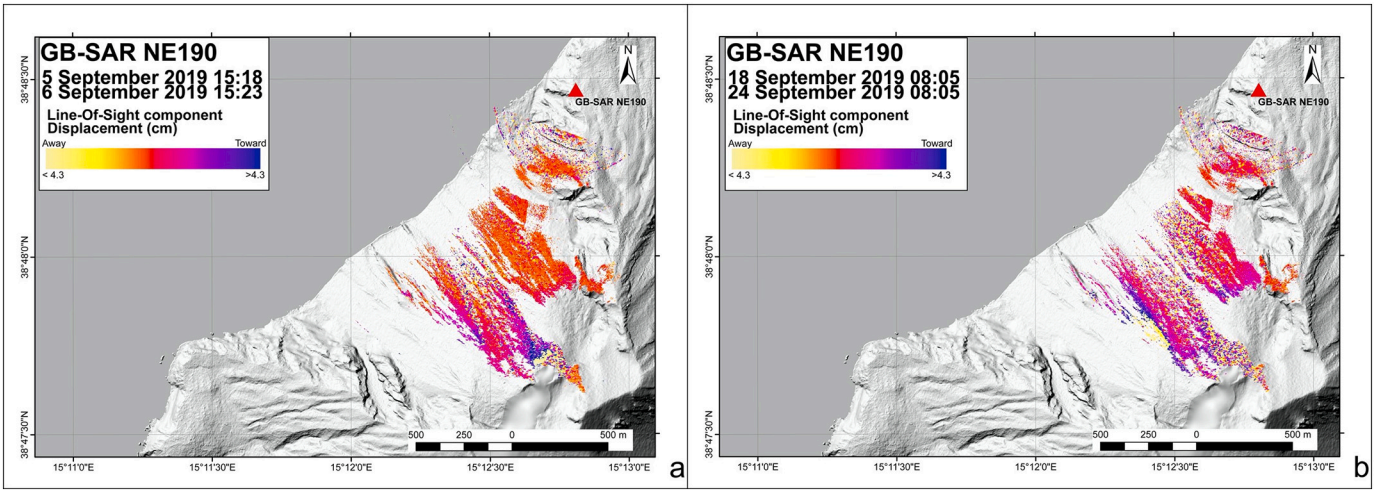

Fig. 10. Interferograms collected on a) 5th September 2019 (15:18 UTC)- 6th September 2019 (15:23 UTC) and b) 18th September 2019 (08:05 UTC) - 24th September 2019 (08:05 UTC), highlighting the displacement related to slope instability in the Sciara del Fuoco and NE crater areas.

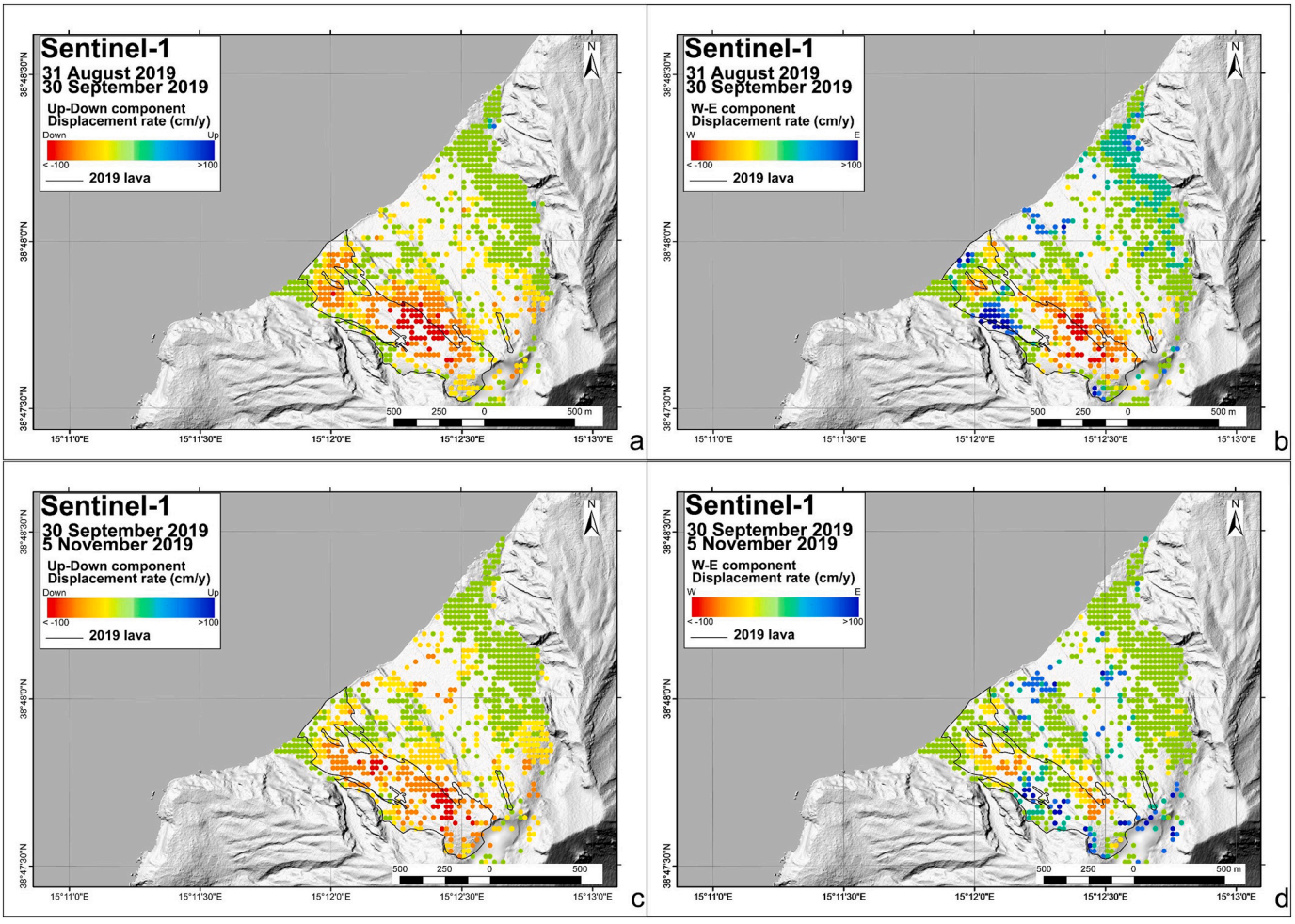

Fig. 11. Post-eruptive Sentinel-1 displacement: 31st August 2019 – 30th September 2019 a) Up-Down component (red dots: subsidence; blue dots: uplift); b) E-W component (red dots: westward displacement; blue dots: eastward displacement); 30th September 2019 – 5th November 2019 c) Up-Down component (red dots: subsidence; blue dots: uplift); d) E-W component (red dots: westward displacement; blue dots: eastward displacement).

and ground systems.

In Fig. 11 we show the S-1 InSAR results relevant to the vertical (Fig. 11a and c) and East-West (Fig. 11b and d) deformation components of two consecutive time intervals (31st August 2019 – 30th September 2019; 30th September 2019 – 5th November 2019), included in the post-eruptive period. We identified these two periods because we observed that the 6-days interferograms covering the 31st August 2019 - 30th September 2019 time interval are characterized by the presence of higher fringe rates with respect to the 30th September 2019 – 5th November 2019 interval (see Fig. S3 of the supplementary material). This fringe rate decrease reveals a progressive reduction of the deformation in time. Maps of Fig. 11 reveal that almost the entire part of the SdF affected by the accumulation of the 2019 lava flow field was deforming. The analysis of these components shows that most of the movement has both a downward (higher than 150 cm/yr in the first time interval) and westward (higher than 100 cm/yr in the same period) direction, compatible with the adjustment of the lava field along the SdF slope. Exceptions to this trend are proximal areas covered by the 2019 lava flow field, and in particular, the zone characterized by pre-effusive low topographic gradient below the SW crater. The calculated noise level outside the SdF was of about 12 cm/yr which is well below the computed maximum values of the displacement rates.

7. Discussion

In this paper we investigated the surface dynamics of Stromboli volcano by using an unprecedented set of space-borne and ground-based SAR data. In particular, we exploited the data collected from April 2015 up to November 2019 along two (one ascending and one descending) Sentinel-1 tracks, as well as the images acquired, in the same period, by two ground-based systems installed along the SdF northern rim. In particular, in our analysis we focused on three different periods: April 2015–June 2019; 3rd July 2019 – 30th August 2019; 31st August 2019 – 5th November 2019. For these three periods we jointly exploited InSAR measurements generated by both space-borne and ground-based systems, thus confirming their complementarity for the mapping and interpretation of the deformation phenomena affecting the Stromboli volcano. In particular, for the first period (April 2015–June 2019) we retrieve the 3D deformation field within the Sciara del Fuoco, by exploiting the ascending and descending satellite long-term MT-InSAR measurements and those achieved through the GB-SAR NE190 system. Indeed, the satellite systems moving over polar-orbits only permit to retrieve the vertical and East-West displacement component (by combing the results from ascending and descending orbits) being totally blind to the displacements along the North-South direction. Instead, the orientation flexibility of the GB-SAR system with respect to the satellite one allows us to have information also along the North-South direction. This further confirms the need to dispose of multiple, complementary systems to overcome the respective space and terrestrial SAR system's limitations, thus increasing the amount of information that can be collected over an area under study. This is even more evident in case of phenomena that cannot be monitored by one of the two systems. A clear example is given by the sin-eruptive period (3rd July 2019 – 30th August 2019), which is characterized by very rapid (in the order of minutes/hours) deformation episodes that cannot be detected with the weekly S-1 temporal sampling, while they can be effectively imaged by the ground-based technologies. On the other hand, the deformation field associated to the 31st August 2019 – 5th November 2019 period has been studied thanks to the S-1 data, being located mainly outside the GB-SAR sensed area.

We remark that most of the ground displacements recorded in the long-term period (April 2015–June 2019) can be explained by comparing them with the morphological changes induced by the previous eruptive activity, mainly the 2010–2011 overflows from the SW crater and the 2014 lava flow field (Fig. 2c, d; Di Traglia et al., 2020). First of all, it should be considered that the S-1 measurements show an area characterized by a persistent low coherence in the central part of the SdF (see Fig. 4) related to the rapid erosion/transport/accumulation processes that occurred in the SdF as response to both explosive activity and erosion/deposition processes (Fig. 2c, d; Bonforte et al., 2016; Di Traglia et al., 2018a, 2020). The along the slope displacements measured in the 2014 lava flow field testifies the persistent motion (creep) induced by slope overloading after effusive activity (Di Traglia et al., 2018a, 2018b). During the same period, the GB-SARs recorded variable displacement in the crater terrace, mainly related to magma movement beneath it. In this period, characterized by the re-awakening eruptive activity after the 2014 flank eruption (Giudicepietro et al., 2020), increasing displacement rates were recorded in the December 2017 – January 2018 and December 2018 – January 2019 time intervals, with the inflation of the summit crater terrace and a small and frequent sliding of the newly emplaced material (Schaefer et al., 2019; Calvari et al., 2021).

A strong inflation of the crater terrace occurred on 3rd July 2019 and lasted ~2 h before the event, whereas no associated deformations were recorded by the GB-SAR devices before the 28th August 2019 explosion, as was the case for the explosion of 5th April 2003 and 15th March 2007 (Antonello et al., 2004; Casagli et al., 2009). During all these paroxysmal events, no sin-explosive deformation was recorded by the GB-SAR due to the scene decorrelation (contrary to what other ground deformation monitoring systems have recorded, i.e. Mattia et al., 2004; Bonaccorso et al., 2009; Giudicepietro et al., 2020; Ripepe et al., 2021; Viccaro et al., 2021), that is consistent with an excessive variation of the scattering properties of the ground. Moreover, the temporal sampling of GB-SARs is much smaller than those of other sensors such as tiltmeters, GNSS, dilatometers, strainmeters, and therefore less suitable for recording transient phenomena of short duration such as Strombolian explosions (see Calvari et al., 2021 on this topic). Further analysis is needed to understand the difference between the 3rd July 2019 and the other three paroxysms that occurred since 2003.

As said before, the strong explosion occurred on 3rd July 2019 changed significantly the electromagnetic properties in much of the island of Stromboli. Accordingly, S-1 interferograms were not useful to measure ground deformation during the 3rd July 2019 paroxysm, even if the SAR coherence was suitable to map the area impacted by both tephra fallout and explosions-triggered wildfires.

The effusive activity as a whole was not associated with signs of inflation and deflation of the crater terrace, as was the case for the 2007 and 2014 eruptions (Casagli et al., 2009; Di Traglia et al., 2018c). Despite this, brief signs of inflation-deflation were associated with the final part of the effusion (29th - 30th August 2019). These short crater terrace inflation-deflation signals, in Stromboli, have been associated with overflows, as the one occurred in 12th January 2013 (Calvari et al., 2016).

Finally, in the last analysed period (31st August 2019 – 5th November 2019), ground displacements were mainly related to instability of the newly emplaced material on the steep volcano slopes. High topographic gradient in the SdF area and around the crater terrace accounted for the large deformations recorded by both systems, similar to the displacement recorded before the 2019 eruption on the 2010–2011 overflows and 2014 lava flow field. However, the proximal 2019 lava flow field is characterized by ground subsidence, accompanied by westward movement, which suggests the possible link between displacements and cooling in the areas with greater lava thickness and/or pre-eruptive low topographic gradient (as proposed by Schaefer et al., 2019 for the proximal areas of the 2014 lava flow field).

8. Conclusions

In the presented analysis a 2015–2019 SAR image dataset acquired by the Sentinel-1 constellation and two GB-SAR systems installed at Stromboli volcano have been processed through InSAR techniques, and the achieved results effectively integrated. In particular, this data

integration consisted of both a 3D displacement field retrieval operation (April 2015–June 2019), and a complementary exploitation (July 2019–November 2019). The former activity allowed for the reconstruction of the slope displacements in between of the 2014 and the 2019 eruptions, whereas the latter was carried out to constrain the eruptive dynamics and the post-eruptive slope readjustment. We remark that, while the InSAR measurements related to slope movements are due to both persistent flank motion and erosion/accumulation of volcaniclastics, the measured displacements associated with the eruptions are related to the magma movement in the shallow storage system. Moreover, we found that the displacement recorded in the crater terrace of Stromboli was characterized by movements toward and away the sensor, consistent with either inflation or deflation of the deformation source respectively. Accordingly, future studies based on the inversion of deformation measurements will be focused on quantifying both the inflation before the 3rd July 2019 paroxysms, and the inflation/deflation associated with the last lava flow, between 29th and 30th August 2019.

This work demonstrates the need to dispose of multiple, complementary SAR systems to increase the amount of InSAR information that can be retrieved for investigating an area, as for the Stromboli case described in this paper. This is particularly critical in zones prone to natural hazards where as much as possible complete information on the occurred displacements should be collected and provided to the civil protection authorities to analyse, monitor and manage the related risk.

Author contributions

Federico Di Traglia: conceptualization, methodology, GB-SAR data curation, writing - original draft preparation, writing - review & editing, visualization, supervision. *Claudio De Luca*: conceptualization, methodology, software, S-1 data curation, S-1 and GB-SAR data integration, writing - original draft preparation, writing - review & editing, visualization. CdL and FdT equally contributed to the paper. *Mariarosaria Manzo*: conceptualization, methodology, S-1 data curation, writing - original draft preparation, writing - review & editing, funding. *Teresa Nolesini*: conceptualization, methodology, GB-SAR data curation, GB-SAR devices management. *Nicola Casagli*: conceptualization, supervision, funding. *Riccardo Lanari*: conceptualization, writing - review & editing, supervision, funding. *Francesco Casu*: conceptualization, methodology, S-1 data curation, writing - original draft preparation, writing - review & editing, supervision, funding. All authors have read and agreed to the submitted version of the manuscript.

Funding

This research was funded by the “Presidenza del Consiglio dei Ministri–Dipartimento della Protezione Civile” (Presidency of the Council of Ministers–Department of Civil Protection), through the IREA-DPC and UniFi-DPC respective agreements, the I-AMICA (PONa3_00363) project, and the EPOS-SP projects of the European Union Horizon 2020 for Research and Innovation Program under Grant 871121.

Declaration of competing interest

The authors declare that they have no known competing financial interests or personal relationships that could have appeared to influence the work reported in this paper.

Acknowledgments

The contents of this paper represent the authors’ ideas and do not necessarily correspond to the official opinion and policies of the “Presidenza del Consiglio dei Ministri–Dipartimento della Protezione Civile” (Presidency of the Council of Ministers–Department of Civil Protection). For scientific, technical, logistic support we thank: (DPC staff) Luigi Coppola, Domenico Mangione, Damiano Piselli, Antonio Ricciardi, Salvatore Zaia, Chiara Cardaci; (PC - Regione Siciliana staff) Nicola Allerruzzo, Filippo Bonvegna, Salvo Di Mauro, Francesco Impellizzeri; (UNIFI staff) Tommaso Carlà, Mattia Ceccatelli, Matteo Del Soldato, Giulia Dotta, Teresa Gracchi, Elena Benedetta Masi, Veronica Pazzi, Lorenzo Solari, Carlo Tacconi Stefanelli, Luca Tanteri, Agnese Turchi; (Ellegi srl LiSALab) Davide Leva, Carlo Rivolta, Ivan Binda Rossetti; (IREA staff) Michele Manunta, Giovanni Onorato, Manuela Bonano, Ivana Zinno, Pietro Tizzani, Vincenzo de Novellis, Emanuela Valerio, Susi Pepe, Giuseppe Solaro, Raffaele Castaldo, Simone Guarino, Ferdinando Parisi, Maria Consiglia Rasulo. The Sentinel-1 data have been provided through the Copernicus Program of the European Union. The DEM of the investigated zone was acquired through the SRTM archive.

The Associate Editor and two anonymous reviewers are thanked for their comments and corrections which helped implement the text. FeDiT would like to particularly thank Elisabetta Del Bello, Sonia Calvari, Flora Giudicepietro, Alessandro Bonaccorso and Giovanni Macedonio, for the discussions on Strombolian activity.

Appendix A. Supplementary data

Supplementary data to this article can be found online at https://doi.org/10.1016/j.rse.2021.112441.

References

Amelung, F., Day, S., 2002. InSAR observations of the 1995 Fogo, Cape Verde, eruption: implications for the effects of collapse events upon island volcanoes. Geophys. Res. Lett. 29 (12), 47–1.

Antonello, G., Casagli, N., Farina, P., Leva, D., Nico, G., Sieber, A.J., Tarchi, D., 2004. Ground-based SAR interferometry for monitoring mass movements. Landslides 1 (1), 21–28.

Barberi, F., Rosi, M., Sodi, A., 1993. Volcanic hazard assessment at Stromboli based on review of historical data. Acta Vulcanol. 3, 173–187.

Bardi, F., Raspini, F., Ciampalini, A., Kristensen, L., Rouyet, L., Lauknes, T.R., Casagli, N., 2016. Space-borne and ground-based InSAR data integration: the Åknes test site. Remote Sens. 8 (3), 237.

Bechor, N.B., Zebker, H.A., 2006. Measuring two-dimensional movements using a single InSAR pair. Geophys. Res. Lett. 33 (16).

Berardino, P., Fornaro, G., Lanari, R., Sansosti, E., 2002. A new algorithm for surface deformation monitoring based on small baseline differential SAR Interferograms. IEEE Trans. Geosci. Remote Sens. 40, 2375–2383.

Bevilacqua, A., Bertagnini, A., Pompilio, M., Landi, P., Del Carlo, P., Di Roberto, A., Aspinal, W., Neri, A., 2020. Major explosions and paroxysms at Stromboli (Italy): a new historical catalog and temporal models of occurrence with uncertainty quantification. Sci. Rep. 10 (1), 1–18.

Biggs, J., Wright, T.J., 2020. How satellite InSAR has grown from opportunistic science to routine monitoring over the last decade. Nat. Commun. 11 (1), 1–4.

Biggs, J., Ebmeier, S.K., Aspinall, W.P., Lu, Z., Pritchard, M.E., Sparks, R.S.J., Mather, T. A., 2014. Global link between deformation and volcanic eruption quantified by satellite imagery. Nat. Commun. 5 (1), 1–7.

Blackburn, E.A., Wilson, L., Sparks, R.J., 1976. Mechanisms and dynamics of strombolian activity. J. Geol. Soc. 132 (4), 429–440.

Bonaccorso, A., Bonforte, A., Gambino, S., Mattia, M., Guglielmino, F., Puglisi, G., Boschi, E., 2009. Insight on recent Stromboli eruption inferred from terrestrial and satellite ground deformation measurements. J. Volcanol. Geotherm. Res. 182 (3–4), 172–181.

Bonano, M., Manzo, M., Casu, F., Manunta, M., Lanari, R., 2016. DInSAR for the monitoring of cultural heritage sites. In: Masini, N., Soldovieri, F. (Eds.), Sensing the Past (Geotechnologies and the Environment). Springer, Cham, Switzerland, pp. 117–134, 2016, ch. 6.

Bonforte, A., Guglielmino, F., 2015. Very shallow dyke intrusion and potential slope failure imaged by ground deformation: the 28 December 2014 eruption on Mount Etna. Geophys. Res. Lett. 42 (8), 2727–2733.

Bonforte, A., Guglielmino, F., Coltelli, M., Ferretti, A., Puglisi, G., 2011. Structural assessment of Mount Etna volcano from permanent Scatterers analysis. Geochem. Geophys. Geosyst. 12 (2).

Bonforte, A., González, P.J., Fernández, J., 2016. Joint terrestrial and aerial measurements to study ground deformation: application to the Sciara Del Fuoco at the Stromboli Volcano (Sicily). Remote Sens. 8 (6), 463.

Borgia, A., Lanari, R., Sansosti, E., Tesauro, M., Berardino, P., Fornaro, G., Neri, M., Murray, J.B., 2000. Actively growing anticlines beneath Catania from the distal motion of Mount Etna’s decollement measured by SAR interferometry and GPS. Geophys. Res. Lett. 27 (20), 3409–3412.

Borgia, A., Tizzani, P., Solaro, G., Manzo, M., Casu, F., Luongo, G., Pepe, A., Berardino, P., Fornaro, G., Sansosti, E., Ricciardi, G.P., Fusi, N., Di Donna, G., Lanari, R., 2005. Volcanic spreading of Vesuvius, a new paradigm for interpreting its volcanic activity. Geophys. Res. Lett. 32 (3).

Calò, F., Ardizzone, F., Castaldo, R., Lollino, P., Tizzani, P., Guzzetti, F., Lanari, R., Angeli, M.-G., Pontoni, F., Manunta, M., 2014. Enhanced landslide investigations through advanced DInSAR techniques: the Ivancich case study, Assisi, Italy. Remote Sens. Environ. 142, 69–82.

Calvari, S., Bonaccorso, A., Madonia, P., Neri, M., Liuzzo, M., Salerno, G.G., Behncke, B., Caltabiano, T., Cristaldi, A., Giuffrida, G., La Spina, A., Marotta, E., Ricci, T., Spampinato, L., 2014. Major eruptive style changes induced by structural modifications of a shallow conduit system: the 2007–2012 Stromboli case. Bull. Volcanol. 76 (7), 841.

Calvari, S., Intrieri, E., Di Traglia, F., Bonaccorso, A., Casagli, N., Cristaldi, A., 2016. Monitoring crater-wall collapse at active volcanoes: a study of the 12 January 2013 event at Stromboli. Bull. Volcanol. 78 (5), 39.

Calvari, S., Di Traglia, F., Ganci, G., Giudicepietro, F., Macedonio, G., Cappello, A., Nolesini, T., Pecora, E., Bilotta, G., Centorrino, V., Corradino, C., Casagli, N., Del Negro, C., 2020. Overflows and pyroclastic density currents in march-April 2020 at Stromboli volcano detected by remote sensing and seismic monitoring data. Remote Sens. 12 (18), 3010.

Calvari, S., Giudicepietro, F., Di Traglia, F., Bonaccorso, A., Macedonio, G., Casagli, N., 2021. Variable magnitude and intensity of Strombolian explosions: focus on the eruptive processes for a first classification scheme for Stromboli volcano (Italy). Remote Sens. 13 (5), 944.

Carlà, T., Intrieri, E., Di Traglia, F., Casagli, N., 2016a. A statistical-based approach for determining the intensity of unrest phases at Stromboli volcano (southern Italy) using one-step-ahead forecasts of displacement time series. Nat. Hazards 84 (1), 669–683.

Carlà, T., Intrieri, E., Di Traglia, F., Nolesini, T., Gigli, G., Casagli, N., 2016b. Guidelines on the use of inverse velocity method as a tool for setting alarm thresholds and forecasting landslides and structure collapses. Landslides 14 (2), 517–534.

Casagli, N., Tibaldi, A., Merri, A., Del Ventisette, C., Apuani, T., Guerri, L., Fortuny-Guasch, J., Tarchi, D., 2009. Deformation of Stromboli Volcano (Italy) during the 2007 eruption revealed by radar interferometry, numerical modelling and structural geological field data. J. Volcanol. Geotherm. Res. 182 (3–4), 182–200.

Casalbore, D., Romagnoli, C., Chiocci, F., Frezza, V., 2010. Morpho-sedimentary characteristics of the volcaniclastic apron around Stromboli volcano (Italy). Mar. Geol. 269 (3–4), 132–148.

Casalbore, D., Romagnoli, C., Bosman, A., Chiocci, F.L., 2011. Potential tsunamigenic landslides at Stromboli Volcano (Italy): insight from marine DEM analysis. Geomorphology 126 (1–2), 42–50.

Casu, F., Manconi, A., 2016. Four-dimensional surface evolution of active rifting from spaceborne SAR data. Geosphere 2016. https://doi.org/10.1130/GES01225.1.

Casu, F., Manzo, M., Lanari, R., 2006. A quantitative assessment of the SBAS algorithm performance for surface deformation retrieval from DInSAR data. Remote Sens. Environ. 102 (3–4), 195–210.

Casu, F., Manconi, A., Pepe, A., Lanari, R., 2011. Deformation time-series generation in areas characterized by large displacement dynamics: the SAR amplitude pixel-offset SBAS technique. IEEE Trans. Geosci. Remote Sens. 49 (7), 2752–2763.

Casu, F., Elefante, S., Imperatore, P., Zinno, I., Manunta, M., De Luca, C., Lanari, R., 2014. SBAS-DInSAR parallel processing for deformation time-series computation. IEEE J. Sel. Top. Appl. Earth Obs. Remote Sens. 7 (8), 3285–3296.

Chaussard, E., 2016. Subsidence in the Parícutin lava field: causes and implications for interpretation of deformation fields at volcanoes. J. Volcanol. Geotherm. Res. 320, 1–11.

Chaussard, E., Amelung, F., 2012. Precursory inflation of shallow magma reservoirs at west Sunda volcanoes detected by InSAR. Geophys. Res. Lett. 39 (21).

Chen, Y., Remy, D., Froger, J.L., Peltier, A., Villeneuve, N., Darrozes, J., Perfettini, H., Bonvalot, S., 2017. Long-term ground displacement observations using InSAR and GNSS at Piton de la Fournaise volcano between 2009 and 2014. Remote Sens. Environ. 194, 230–247.

Chen, Y., Zhang, K., Froger, J.L., Tan, K., Remy, D., Darrozes, J., Peltier, A., Feng, X., Li, H., Villeneuve, N., 2018. Long-term subsidence in lava fields at piton de la Fournaise volcano measured by InSAR: new insights for interpretation of the eastern flank motion. Remote Sens. 10 (4), 597.

Curlander, J.C., McDonough, R.N., 1991. Synthetic Aperture Radar Systems and Signal Processing. Wiley-Interscience, New York.

D'Auria, L., Pepe, S., Castaldo, R., Giudicepietro, F., Macedonio, G., Ricciolino, P., Tizzani, P., Casu, F., Lanari, R., Manzo, M., Martini, M., Sansosti, E., Zinno, I., 2015. Magma injection beneath the urban area of Naples: a new mechanism for the 2012-2013 volcanic unrest at Campi Flegrei caldera. Sci. Rep. 5, 13100. https://doi.org/10.1038/srep13100.

De Luca, C., Zinno, I., Manunta, M., Lanari, R., Casu, F., 2017. Large areas surface deformation analysis through a cloud computing P-SBAS approach for massive processing of DInSAR time series. Remote Sens. Environ. 202, 3–17. Dec. 2017.

Dematteis, N., Luzi, G., Giordan, D., Zucca, F., Allasia, P., 2017. Monitoring Alpine glacier surface deformations with GB-SAR. Remote Sens. Lett. 8 (10), 947–956.

Di Traglia, F., Nolesini, T., Intrieri, E., Mugnai, F., Leva, D., Rosi, M., Casagli, N., 2014a. Review of ten years of volcano deformations recorded by the ground-based InSAR monitoring system at Stromboli volcano: a tool to mitigate volcano flank dynamics and intense volcanic activity. Earth Sci. Rev. 139, 317–335.

Di Traglia, F., Cauchie, L., Casagli, N., Saccorotti, G., 2014b. Decrypting geophysical signals at Stromboli Volcano (Italy): integration of seismic and Ground-Based InSAR displacement data. Geophys. Res. Lett. 41 (8), 2753–2761.

Di Traglia, F., Battaglia, M., Nolesini, T., Lagomarsino, D., Casagli, N., 2015. Shifts in the eruptive styles at Stromboli in 2010–2014 revealed by ground-based InSAR data. Sci. Rep. 5, 13569.

Di Traglia, F., Nolesini, T., Ciampalini, A., Solari, L., Frodella, W., Bellotti, F., Fumagalli, A., De Rosa, G., Casagli, N., 2018a. Tracking morphological changes and slope instability using spaceborne and ground-based SAR data. Geomorphology 300, 95–112.

Di Traglia, F., Nolesini, T., Solari, L., Ciampalini, A., Frodella, W., Steri, D., Allotta, B., Rindi, A., Marini, L., Monni, N., Galardi, E., Casagli, N., 2018b. Lava delta deformation as a proxy for submarine slope instability. Earth Planet. Sci. Lett. 488, 46–58.

Di Traglia, F., Calvari, S., D'Auria, L., Nolesini, T., Bonaccorso, A., Fornaciai, A., Esposito, A., Favalli, M., Cristaldi, A., Casagli, N., 2018c. The 2014 effusive eruption at Stromboli: new insights from in situ and remote-sensing measurements. Remote Sens. 10 (12), 2035.

Di Traglia, F., Bartolini, S., Artesi, E., Nolesini, T., Ciampalini, A., Lagomarsino, D., Martí, J., Casagli, N., 2018d. Susceptibility of intrusion-related landslides at volcanic islands: the Stromboli case study. Landslides 15 (1), 21–29.

Di Traglia, F., Fornaciai, A., Favalli, M., Nolesini, T., Casagli, N., 2020. Catching geomorphological response to volcanic activity on steep slope volcanoes using multi-platform remote sensing. Remote Sens. 12 (3), 438.

Dumont, S., Sigmundsson, F., Parks, M.M., Drouin, V.J., Pedersen, G., Jónsdóttir, I., Höskuldsson, Á., Hooper, A., Spaans, K., Bagnardi, M., Gudmundsson, M.T., Barsotti, S., Jónsdóttir, K., Högnadóttir, T., Magnússon, E., Hjartardóttir, Á.R., Dürig, T., Rossi, C., Oddsson, B., 2018. Integration of SAR data into monitoring of the 2014–2015 Holuhraun eruption, Iceland: contribution of the icelandic volcanoes supersite and the FutureVolc projects. Front. Earth Sci. 6, 231.

Dzurisin, D., Lu, Z., Poland, M.P., Wicks, C.W., 2019. Space-based imaging radar studies of US volcanoes. Front. Earth Sci. 6, 249.

Ebmeier, S.K., Andrews, B.J., Araya, M.C., Arnold, D.W.D., Biggs, J., Cooper, C., Cottrell, E., Furtney, M., Hickey, J., Jay, J., Lloyd, R., Parker, A.L., Pritchard, M.E., Robertson, E., Venzke, E., Williamson, J.L., 2018. Synthesis of global satellite observations of magmatic and volcanic deformation: implications for volcano monitoring & the lateral extent of magmatic domains. J. Appl. Volcanol. 7 (1), 2.

Elachi, C., 1988. Spaceborne Radar Remote Sensing: Applications and Techniques. IEEE, New York, 285 p.

Fernández, J., Yu, T.T., Rodrıguez-Velasco, G., González-Matesanz, J., Romero, R., Rodrıguez, G., Quirós, R., Dalda, A., Aparicio, A., Blanco, M.J., 2003. New geodetic monitoring system in the volcanic island of Tenerife, canaries, Spain. Combination of InSAR and GPS techniques. J. Volcanol. Geotherm. Res. 124 (3–4), 241–253.

Ferretti, A., Prati, C., Rocca, F., 2001. Permanent scatterers in SAR interferometry. IEEE Trans. Geosci. Remote Sens. 39 (1), 8–20.

Fialko, Y., 2004. Evidence of fluid-filled upper crust from observations of post-seismic deformation due to the 1992 Mw7.3 Landers earthquake. J. Geophys. Res. 109, B08401. https://doi.org/10.1029/2003JB002985.

Fialko, Y., Simons, M., 2001. Evidence for on-going inflation of the Socorro magma body, New Mexico, from interferometric synthetic aperture radar imaging. Geophys. Res. Lett. 28, 3549–3552.

Fornaciai, A., Favalli, M., Nannipieri, L., 2019. Numerical simulation of the tsunamis generated by the Sciara del Fuoco landslides (Stromboli Island, Italy). Sci. Rep. 9 (1), 1–12.

Francalanci, L., Lucchi, F., Keller, J., De Astis, G., Tranne, C.A., 2013. Eruptive, volcano-tectonic and magmatic history of the Stromboli volcano (north-eastern Aeolian archipelago). Geol. Soc. Lond. Mem. 37 (1), 397–471.

Franceschetti, G., Lanari, R., 1999. Synthetic Aperture Radar Processing. CRC Press, Boca Raton, FL, USA.

Frodella, W., Ciampalini, A., Bardi, F., Salvatici, T., Di Traglia, F., Basile, G., Casagli, N., 2018. A method for assessing and managing landslide residual hazard in urban areas. Landslides 15 (2), 183–197.

Froger, J.L., Famin, V., Cayol, V., Augier, A., Michon, L., Lénat, J.F., 2015. Time-dependent displacements during and after the April 2007 eruption of Piton de la Fournaise, revealed by interferometric data. J. Volcanol. Geotherm. Res. 296, 55–68.

Gabriel, A.K., Goldstein, R.M., Zebker, H.A., 1989. Mapping small elevation changes over large areas: differential interferometry. J. Geophys. Res. 94, 9183–9191. https://doi.org/10.1029/JB094iB07p09183.

Garthwaite, M.C., Miller, V.L., Saunders, S., Parks, M.M., Hu, G., Parker, A.L., 2019. A simplified approach to operational InSAR monitoring of volcano deformation in low-and middle-income countries: case study of Rabaul caldera, Papua New Guinea. Front. Earth Sci. 6, 240.

Giordano, G., De Astis, G., 2021. The summer 2019 basaltic Vulcanian eruptions (paroxysms) of Stromboli. Bull. Volcanol. 83 (1), 1–27.

Giudicepietro, F., Calvari, S., Alparone, S., Bianco, F., Bonaccorso, A., Bruno, V., Caputo, T., Cristaldi, A., D'Auria, L., De Cesare, W., Di Lieto, B., Esposito, A.M., Gambino, S., Inguaggiato, S., Macedonio, G., Martini, M., Mattia, M., Orazi, M., Paonita, A., Peluso, R., Privitera, E., Romano, P., Scarpato, G., Tramelli, A., Vita, F., 2019. Integration of ground-based remote-sensing and in situ multidisciplinary monitoring data to analyze the eruptive activity of Stromboli Volcano in 2017–2018. Remote Sens. 11 (15), 1813.

Giudicepietro, F., López, C., Macedonio, G., Alparone, S., Bianco, F., Calvari, S., De Cesare, W., Delle Donne, D., Di Lieto, B., Esposito, A.M., Orazi, M., Peluso, R., Privitera, E., Romano, P., Scarpato, G., Tramelli, A., 2020. Geophysical precursors of the July-august 2019 paroxysmal eruptive phase and their implications for Stromboli volcano (Italy) monitoring. Sci. Rep. 10 (1), 1–16.

Guglielmino, F., Nunnari, G., Puglisi, G., Spata, A., 2011. Simultaneous and integrated strain tensor estimation from geodetic and satellite deformation measurements to obtain three-dimensional displacement maps. IEEE Trans. Geosci. Remote Sens. 49 (6), 1815–1826.

Hooper, A., 2008. Amulti-temporal InSARmethod incorporating both persistent scatterer and small baseline approaches. Geophys. Res. Lett. 35, L16302 https://doi.org/10.1029/2008GL034654.

Hu, J., Li, Z.W., Ding, X.L., Zhu, J.J., Zhang, L., Sun, Q., 2014. Resolving three-dimensional surface displacements from InSAR measurements: a review. Earth Sci. Rev. 133, 1–17.

Inguaggiato, S., Vita, F., Cangemi, M., Calderone, L., 2019. Increasing summit degassing at the Stromboli Volcano and relationships with volcanic activity (2016–2018). Geosciences 9 (4), 176.

Inguaggiato, S., Vita, F., Cangemi, M., Calderone, L., 2020. Changes in CO2 soil degassing style as a possible precursor to volcanic activity: the 2019 case of Stromboli paroxysmal eruptions. Appl. Sci. 10 (14), 4757.

Kokelaar, P., Romagnoli, C., 1995. Sector collapse, sedimentation and clast population evolution at an active island-arc volcano: Stromboli, Italy. Bull. Volcanol. 57 (4), 240–262.

Kuraoka, S., Nakashima, Y., Doke, R., Mannen, K., 2018. Monitoring ground deformation of eruption center by ground-based interferometric synthetic aperture radar (GB-InSAR): a case study during the 2015 phreatic eruption of Hakone volcano. Earth Planets Space 70 (1), 1–9.

Lanari, R., Mora, O., Manunta, M., Mallorquí, J.J., Berardino, P., Sansosti, E., 2004a. A small baseline approach for investigating deformations on full resolution differential SAR interferograms. IEEE Trans. Geosci. Remote Sens. 42, 1377–1386.

Lanari, R., Lundgren, P., Manzo, M., Casu, F., 2004b. Satellite radar inter- ferometry time series analysis of surface deformation for Los Angeles, California. Geophys. Res. Lett. 31 (23). L23 613–1–L23 613–5.

Lanari, R., Casu, F., Manzo, M., Zeni, G., Berardino, P., Manunta, M., Pepe, A., 2007a. An overview of the small BAseline subset algorithm: a DInSAR technique for surface deformation analysis. Pure Appl. Geophys. (PAGEOPH) 164 (4), 637–661.

Lanari, R., Casu, F., Manzo, M., Lundgren, P., 2007b. Application of the SBAS-DInSAR technique to fault creep: a case study of the Hayward fault, California. Remote Sens. Environ. 109 (1), 20–28.

Lanari, R., et al., 2010. Surface displacements associated with the L'Aquila 2009 Mw 6.3 earthquake (central Italy): new evidence from SBAS DInSAR time series analysis. Geophys. Res. Lett. 37 (20) https://doi.org/10.1029/2010GL044780, 2010, Art. no. L20309.

Lanari, R., Bonano, M., Casu, F., De Luca, C., Manunta, M., Manzo, M., Onorato, G., Zinno, I., 2020. Automatic generation of Sentinel-1 continental scale DInSAR deformation time series through an extended P-SBAS processing pipeline in a cloud computing environment. Remote Sens. 12, 2961.

Lundgren, P., Casu, F., Manzo, M., Pepe, A., Berardino, P., Sansosti, E., Lanari, R., 2004. Gravity and magma induced spreading of Mount Etna volcano revealed by satellite radar interferometry. Geophys. Res. Lett. 31 (4).

Manunta, M., De Luca, C., Zinno, I., Casu, F., Manzo, M., Bonano, M., Fusco, A., Pepe, A., Onorato, G., Berardino, P., De Martino, P., Lanari, R., 2019. The parallel SBAS approach for Sentinel-1 interferometric wide swath deformation time-series generation: algorithm description and products quality assessment. IEEE Trans. Geosci. Remote Sens. 57 (9) https://doi.org/10.1109/TGRS.2019.2904912.

Manzo, M., Fialko, Y., Casu, F., Pepe, A., Lanari, R., 2012. A quantitative assessment of DInSAR measurements of interseismic deformation: the southern San Andreas fault case study. Pure Appl. Geophys. 169 (8), 1463–1482.

Maramai, A., Graziani, L., Tinti, S., 2005. Tsunamis in the Aeolian Islands (southern Italy): a review. Mar. Geol. 215 (1–2), 11–21.

Marsella, M., Baldi, P., Coltelli, M., Fabris, M., 2012. The morphological evolution of the Sciara del Fuoco since 1868: reconstructing the effusive activity at Stromboli volcano. Bull. Volcanol. 74 (1), 231–248.

Massonnet, D., Rossi, M., Carmona, C., Adragna, F., Peltzer, G., Feigl, K., Rabaute, T., 1993. The displacement field of the landers earthquake mapped by radar interferometry. Nature 364 (6433), 138–142.

Massonnet, D., Briole, P., Arnaud, A., 1995. Deflation of Mount Etna monitored by spaceborne radar interferometry. Nature 375, 567–570.

Mattia, M., Rossi, M., Guglielmino, F., Aloisi, M., Bock, Y., 2004. The shallow plumbing system of Stromboli Island as imaged from 1 Hz instantaneous GPS positions. Geophys. Res. Lett. 31, L24610 https://doi.org/10.1029/2004GL021281.

McAlpin, D.B., Meyer, F.J., Gong, W., Beget, J.E., Webley, P.W., 2017. Pyroclastic flow deposits and InSAR: analysis of long-term subsidence at Augustine volcano, Alaska. Remote Sens. 9 (1), 4.

Métrich, N., Bertagnini, A., Pistolesi, M., 2021. Paroxysms at Stromboli volcano (Italy): source, genesis and dynamics. Front. Earth Sci. 9, 45.

Monserrat, O., Crosetto, M., Luzi, G., 2014. A review of ground-based SAR interferometry for deformation measurement. ISPRS J. Photogramm. Remote Sens. 93, 40–48.

Muller, C., del Potro, R., Biggs, J., Gottsmann, J., Ebmeier, S.K., Guillaume, S., Cattin, P.-H., Van der Laat, R., 2015. Integrated velocity field from ground and satellite geodetic techniques: application to Arenal volcano. Geophys. J. Int. 200 (2), 863–879.

Narita, S., Murakami, M., 2018. Shallow hydrothermal reservoir inferred from post-eruptive deflation at Ontake volcano as revealed by PALSAR-2 InSAR. Earth Planets Space 70 (1), 1–12.

Nave, R., Isaia, R., Vilardo, G., Barclay, J., 2010. Re-assessing volcanic hazard maps for improving volcanic risk communication: application to Stromboli Island, Italy. J. Maps 6 (1), 260–269.

Neri, M., Casu, F., Acocella, V., Solaro, G., Pepe, S., Berardino, P., Sansosti, E., Caltabianco, T., Lundgren, P., Lanari, R., 2009. Deformation and eruptions at Mt. Etna (Italy): a lesson from 15 years of observations. Geophys. Res. Lett. 36 https://doi.org/10.1029/2008GL036151. ISSN: 0094-8276.

Peltzer, G., Rosen, P.A., 1995. Surface displacement of the 17 May 1993 Eureka Valley earthquake observed by SAR interferometry. Science 268, 1333–1336.

Peltzer, G., Crampe, F., Hensley, S., Rosen, P., 2001. Transient strain accumulation and fault interaction in the Eastern California Shear Zone. Geology 29, 975–978.

Pinel, V., Poland, M.P., Hooper, A., 2014. Volcanology: lessons learned from synthetic aperture radar imagery. J. Volcanol. Geotherm. Res. 289, 81–113.

Plank, S., Marchese, F., Filizzola, C., Pergola, N., Neri, M., Nolde, M., Martinis, S., 2019. The July/August 2019 lava flows at the Sciara del Fuoco, Stromboli–analysis from multi-sensor infrared satellite imagery. Remote Sens. 11 (23), 2879.

Poland, M.P., Peltier, A., Bonforte, A., Puglisi, G., 2017. The spectrum of persistent volcanic flank instability: a review and proposed framework based on Kīlauea, Piton de la Fournaise, and Etna. J. Volcanol. Geotherm. Res. 339, 63–80.

Pritchard, M.E., Simons, M., 2004. An InSAR-based survey of volcanic deformation in the central Andes. Geochem. Geophys. Geosyst. 5 (2).

Richter, N., Froger, J.L., 2020. The role of interferometric synthetic aperture radar in detecting, mapping, monitoring, and modelling the volcanic activity of piton de la Fournaise, La Réunion: a review. Remote Sens. 12 (6), 1019.

Rignot, E., 1998. Fast recession of a West Antarctic glacier. Science 281, 549–551.

Ripepe, M., Lacanna, G., Pistolesi, M., Silengo, M.C., Aiuppa, A., Laiolo, M., Massimetti, F., Innocenti, L., Della Schiava, M., Bitetto, M., La Monica, F.P., Nishimura, T., Rosi, M., Mangione, D., Ricciardi, A., Genco, R., Coppola, D., Marchetti, E., Delle Donne, D., 2021. Ground deformation reveals the scale-invariant conduit dynamics driving explosive basaltic eruptions. Nat. Commun. 12 (1), 1–8.

Risica, G., Speranza, F., Giordano, G., De Astis, G., Lucchi, F., 2019. Palaeomagnetic dating of the Neostromboli succession. J. Volcanol. Geotherm. Res. 371, 229–244.

Rocca, F., 2003. 3D motion recovery from multi-angle and/or left right interferometry. In: Proceedings of the FRINGE 2003 Workshop (ESA SP-550). ESA/ESRIN, Frascati, Italy, 1–5 December 2003.

Romagnoli, C., Casalbore, D., Chiocci, F.L., Bosman, A., 2009. Offshore evidence of large-scale lateral collapses on the eastern flank of Stromboli, Italy, due to structurally-controlled, bilateral flank instability. Mar. Geol. 262 (1–4), 1–13.

Ruch, J., Pepe, S., Casu, F., Solaro, G., Pepe, A., Acocella, V., Neri, M., Sansosti, E., 2013. Seismo-tectonic behavior of the Pernicana Fault System (Mt Etna): a gauge for volcano flank instability? *J. Geophys. Res.* Solid Earth 118, 4398–4409. https://doi.org/10.1002/jgrb.50281.

Rudolf, H., Leva, D., Tarchi, D., Sieber, A.J., 1999. A mobile and versatile SAR system. In: IEEE 1999 International Geoscience and Remote Sensing Symposium. IGARSS'99 (Cat. No. 99CH36293), 1. IEEE, pp. 592–594.

Sansosti, E., Casu, F., Manzo, M., Lanari, R., 2010. Space-borne radar interferometry techniques for the generation of deformation time series: an advanced tool for Earth's surface displacement analysis. Geophys. Res. Lett. 37, L20305.

Schaefer, L.N., Lu, Z., Oommen, T., 2015. Dramatic volcanic instability revealed by InSAR. Geology 43 (8), 743–746.

Schaefer, L.N., Di Traglia, F., Chaussard, E., Lu, Z., Nolesini, T., Casagli, N., 2019. Monitoring volcano slope instability with Synthetic Aperture Radar: a review and new data from Pacaya (Guatemala) and Stromboli (Italy) volcanoes. Earth-Sci. Rev. 192, 236–257.

Scifoni, S., Bonano, M., Marsella, M., Sonnessa, A., Tagliafierro, V., Manunta, M., Lanari, R., Ojha, C., Sciotti, M., 2016. On the joint exploitation of long-term DInSAR time series and geological information for the investigation of ground settlements in the town of Roma (Italy). Remote Sens. Environ. 182, 113–127. https://doi.org/10.1016/j.rse.2016.04.017.

Smittarello, D., Cayol, V., Pinel, V., Froger, J.L., Peltier, A., Dumont, Q., 2019. Combining InSAR and GNSS to track magma transport at basaltic volcanoes. Remote Sens. 11 (19), 2236.

Tesauro, M., Berardino, P., Lanari, R., Sansosti, E., Fornaro, G., Franceschetti, G., 2000. Urban subsidence inside the city of Napoli (Italy) observed by satellite radar interferometry. Geophys. Res. Lett. 27 (13), 1961–1964.

Tibaldi, A., 2001. Multiple sector collapses at stromboli volcano, Italy: how they work. Bull. Volcanol. 63, 112–125. https://doi.org/10.1007/s004450100129.

Turchi, A., Di Traglia, F., Luti, T., Olori, D., Zetti, I., Fanti, R., 2020. Environmental aftermath of the 2019 Stromboli eruption. Remote Sens. 12 (6), 994.

Viccaro, M., Cannata, A., Cannavò, F., De Rosa, R., Giuffrida, M., Nicotra, E., Petrelli, M., Sacco, G., 2021. Shallow conduit dynamics fuel the unexpected paroxysms of Stromboli volcano during the summer 2019. Sci. Rep. 11 (1), 1–15.

Werner, C., Wegmüller, U., Strozzi, T., Wiesmann, A., 2003. Interferometric point target analysis for deformation mapping. In: Proceedings of the Geoscience and Remote Sensing Symposium, 7, pp. 4362–4364. Toulouse, France, 21–25 July 2003.

Zebker, H.A., Villasenor, J., Sep. 1992. Decorrelation in interferometric radar echoes. IEEE Trans. Geosci. Remote Sens. 30 (5), 950–959.

Zeni, G., Bonano, M., Casu, F., Manunta, M., Manzo, M., Marsella, M., Pepe, A., Lanari, R., 2011. Long term deformation analysis of historical buildings through the advanced SBAS DInSAR technique: the case study of the city of Roma Italy. J. Geophys. Eng. 8, S1. https://doi.org/10.1088/1742-2132/8/3/S01.

Zinno, I., Elefante, S., Mossucca, L., De Luca, C., Manunta, M., Terzo, O., Lanari, R., Casu, F., 2015. A first assessment of the P-SBAS DInSAR algorithm performances

within a cloud computing environment. IEEE J. Sel. Topics Appl. Earth Observ. Remote Sens. 8 (10), 4675–4686.
Zinno, I., Casu, F., De Luca, C., Elefante, S., Lanari, R., Manunta, M., 2017. A cloud computing solution for the efficient implementation of the P-SBAS DInSAR approach. IEEE JSTARS 10 (3), 802–817.
Zinno, I., Bonano, M., Buonanno, S., Casu, F., De Luca, C., Manunta, M., Manzo, M., Lanari, R., 2018. National scale surface deformation time series generation through advanced DInSAR processing of sentinel-1 data within a cloud computing environment. IEEE Trans. Big Data. https://doi.org/10.1109/TBDATA.2018.2863558.

Web references

ESA. Sentinel-1 SAR User Guide—Interferometric Wide Swath. 2018. Available online: https://sentinels.copernicus.eu/web/sentinel/user-guides/sentinel-1-sar/acquisition-modes/interferometric-wide-swath (accessed on 24/01/2019).